Interrogating theoretical models of neural computation with deep inference

Sean R. Bittner, Agostina Palmigiano, Alex T. Piet, Chunyu A. Duan, Francesca Mastrogiuseppe, Srdjan Ostojic, Carlos D. Brody, Kenneth D. Miller, and John P. Cunningham.

1 Abstract

The cornerstone of theoretical neuroscience is the circuit model: a system of equations that captures a hypothesized neural mechanism of scientific importance. Such models are valuable when they give rise to an experimentally observed phenomenon – whether behavioral or in terms of neural activity – and thus can offer insight into neural computation. The operation of these circuits, like all models, critically depends on the choices of model parameters. Historically, the gold standard has been to analytically derive the relationship between model parameters and computational properties. However, this enterprise quickly becomes infeasible as biologically realistic constraints are included into the model, often resulting in *ad hoc* approaches to understanding the relationship between model and computation. We bring recent machine learning techniques – the use of deep generative models for probabilistic inference – to bear on this problem, learning distributions of parameters that produce the specified properties of computation. Importantly, the techniques we introduce offer a principled means to understand the implications of model parameter choices on computational properties of interest. We motivate this methodology with a worked example analyzing sensitivity in the stomatogastric ganglion. We then use it to generate insights into neuron-type input-responsivity in a model of primary visual cortex, a new understanding of rapid task switching in superior colliculus models, and attribution of bias in recurrent neural networks solving a toy mathematical problem. More generally, this work suggests a departure from realism vs tractability considerations, towards the use of modern machine learning for sophisticated interrogation of biologically relevant models.

2 Introduction

The fundamental practice of theoretical neuroscience is to use a mathematical model to understand neural computation, whether that computation enables perception, action, or some intermediate processing [1]. In this field, a neural computation is systematized with a set of equations – the model – and these equations are motivated by biophysics, neurophysiology, and other conceptual considerations. The function of this system is governed by the choice of model parameters, which

when configured appropriately, give rise to a measurable signature of a computation. The work of analyzing a model then becomes the inverse problem: given a computation of interest, how can we reason about these suitable parameter configurations – their likely values, their uniquenesses and degeneracies, their attractor states and phase transitions, and more?

Consider the idealized practice: a theorist considers a model carefully and analytically derives how model parameters govern the computation. Seminal examples of this gold standard include our field's understanding of memory capacity in associative neural networks [2], chaos and autocorrelation timescales in random neural networks [3], and the paradoxical effect in excitatory/inhibitory networks [4]. Unfortunately, as circuit models include more biological realism, theory via analytic derivation becomes intractable. This fact creates an unfavorable tradeoff for the theorist. On the one hand, one may tractably analyze systems of equations with unrealistic assumptions (for example symmetry or gaussianity), producing accurate inferences about parameters of a too-simple model. On the other hand, one may choose a more biologically relevant model at the cost of *ad hoc* approaches to analysis (simply examining simulated activity), producing questionable or partial inferences about parameters of an appropriately complex, scientifically relevant model.

Of course, this same tradeoff has been confronted in many scientific fields and engineering problems characterized by the need to do inference in complex models. In response, the machine learning community has made remarkable progress in recent years, via the use of deep neural networks as a powerful inference engine: a flexible function family that can map observed phenomena (in this case the measurable signal of some computation) back to probability distributions quantifying the likely parameter configurations. One celebrated example of this approach from the machine learning community, from which we draw key inspiration for this work, is the variational autoencoder [5, 6], which uses a deep neural network to induce an (approximate) posterior distribution on hidden variables in a latent variable model, given data. Indeed, these tools have been used to great success in neuroscience as well, in particular for interrogating parameters (sometimes treated as hidden states) in models of both cortical population activity [7, 8, 9, 10] and animal behavior [11, 12, 13]. These works have used deep neural networks to expand the expressivity and accuracy of statistical models of neural data [14].

However, these inference tools have not significantly influenced the study of theoretical neuroscience models, for at least three reasons. First, at a practical level, the nonlinearities and dynamics of many theoretical models are such that conventional inference tools typically produce a narrow set of insights into these models. Indeed, only in the last few years has the deep learning toolkit

expanded to a point of relevance to this class of problem. Second, the object of interest from a theoretical model is not typically data itself, but rather a qualitative phenomenon – inspection of model behavior, or better, a measurable signature of some computation – an *emergent property* of the model. Third, because theoreticians work carefully to construct a model that has biological relevance, such a model as a result often does not fit cleanly into the framing of a statistical model. Technically, because many such models stipulate a noisy system of differential equations that can only be sampled or realized through forward simulation, they lack the explicit likelihood and priors central to the probabilistic modeling toolkit.

To address these three challenges, we developed an inference methodology – 'emergent property inference' – which learns a distribution over parameter configurations in a theoretical model. Critically, this distribution is such that draws from the distribution (parameter configurations) correspond to systems of equations that give rise to a specified emergent property. First, we stipulate a bijective deep neural network that induces a flexible family of probability distributions over model parameterizations with a probability density we can calculate [15, **?**, **?**]. Second, we quantify the notion of emergent properties as a set of moment constraints on datasets generated by the model. Thus, an emergent property is not a single data realization, but a phenomenon or a feature of the model, which is the central object of interest to the theorist (unlike say the statistical neuroscientist). Conditioning on an emergent property requires a variant of deep probabilistic inference methods, which we have previously introduced [16]. Third, because we cannot assume the theoretical model has explicit likelihood on data or the emergent property of interest, we use stochastic gradient techniques in the spirit of likelihood free variational inference [17]. Taken together, emergent property inference (EPI) provides a methodology for inferring and then reasoning about parameter configurations that give rise to particular emergent phenomena in theoretical models. To clarify the technical details of EPI, we use it to analyze network syncing in a classic model of the stomatogastric ganglion [18].

Equipped with this methodology, we then investigated three models of current importance in theoretical neuroscience. These models were chosen to demonstrate generality through ranges of biological realism (conductance-based biophysics to recurrent neural networks), neural system function (pattern generation to abstract cognitive function), and network scale (four to infinite neurons). First, we use EPI to produce a set of verifiable hypotheses of input-responsivity in a four neuron-type dynamical model of primary visual cortex; we then validate these hypotheses in the model. Second, we demonstrated how the systematic application of EPI to levels of task performance can

generate experimentally testable hypotheses regarding connectivity in superior colliculus. Third, we use EPI to uncover the sources of bias in a low-rank recurrent neural network executing a toy mathematical computation. The novel scientific insights offered by EPI contextualize and clarify the previous studies exploring these models [18, 19, 20, 21] and more generally offer a quantitative grounding for theoretical models going forward, pointing a way to how rigorous statistical inference can enhance theoretical neuroscience at large.

We note that, during our preparation and early presentation of this work [22, 23], another work has arisen with broadly similar goals: bringing statistical inference to mechanistic models of neural circuits [24]. We are excited by this broad problem being recognized by the community, and we emphasize that these works offer complementary neuroscientific contributions and use different technical methodologies. Scientifically, our work has focused primarily on systems-level theoretical models, while their focus has been on lower-level cellular models. Secondly, there are several key technical differences in the approaches (see Section A.1.4) perhaps most notably is our focus on the emergent property – the measurable signal of the computation in question, vs their focus on observed datasets; both certainly are worthy pursuits. The existence of these complementary methodologies emphasizes the increased importance and timeliness of both works.

3 Results

3.1 Motivating emergent property inference of theoretical models

Consideration of the typical workflow of theoretical modeling clarifies the need for emergent property inference. First, the theorist designs or chooses an existing model that, it is hypothesized, captures the computation of interest. To ground this process in a well-known example, consider the stomatogastric ganglion (STG) of crustaceans, a small neural circuit which generates multiple rhythmic muscle activation patterns for digestion [25]. A model of the STG [18] is shown schematically in Figure 1A, and note that the behavior of this model will be critically dependent on its parameterization – the choices of conductance parameters $z = [g_{\text{el}}, g_{\text{synA}}]$. Spcecifically, the two fast neurons ($f1$ and $f2$) mutually inhibit one another, and oscillate at a faster frequency than the mutually inhibiting slow neurons ($s1$ and $s2$), and the hub neuron (hub) couples with the fast or slow population or both.

Second, once the model is selected, the theorist defines the emergent property, the measurable signal of scientific interest. To continue our running STG example, one such emergent property

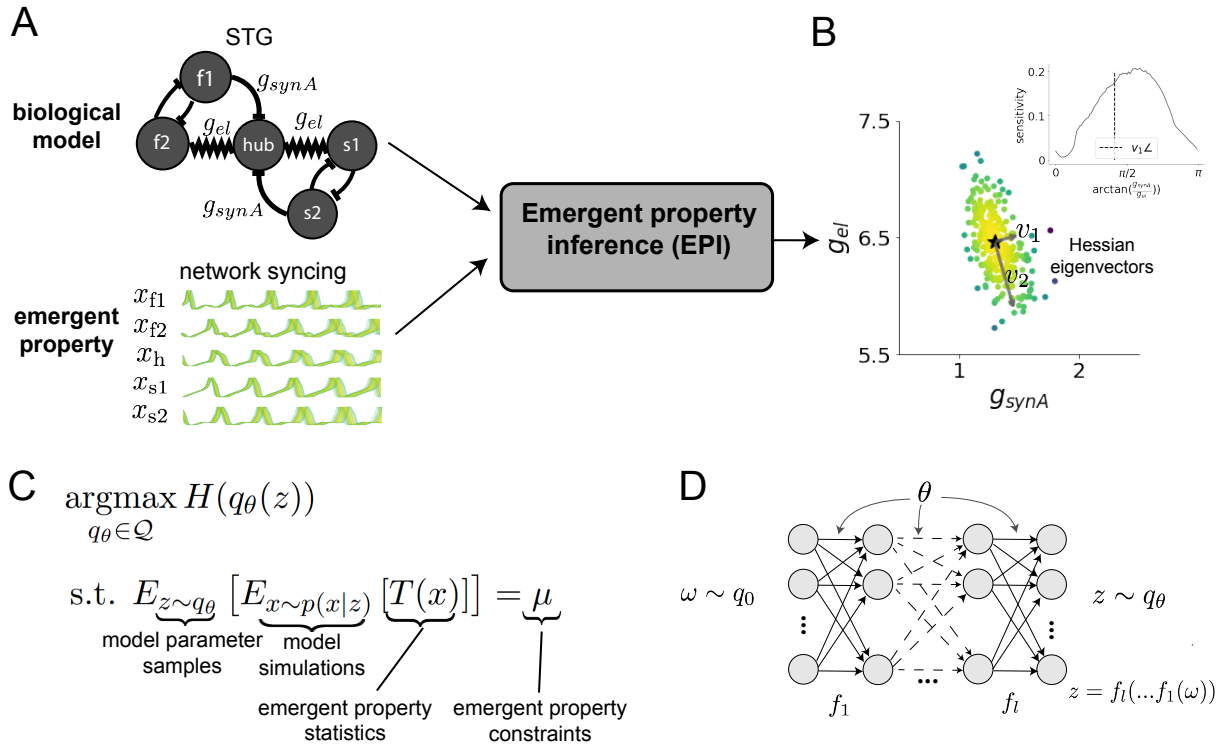

Figure 1: Emergent property inference (EPI) in the stomatogastric ganglion. A. For a choice of model (STG) and emergent property (network syncing), emergent property inference (EPI) learns a posterior distribution of the model parameters $z = [g_{\text{el}}, g_{\text{synA}}]^\top$ conditioned on network syncing. B. An EPI distribution of STG model parameters producing network syncing. The eigenvectors of the Hessian at the mode of the inferred distribution are indicated as v_1 and v_2. (Inset) Sensitivity of the system with respect to network syncing along all dimensions of parameter space away from the mode. (see Section A.2.1). C. EPI learns a distribution $q_\theta(z)$ of model parameters that produce an emergent property: the emergent property statistics $T(x)$ are fixed in expectation over parameter distribution samples $z \sim q_\theta(z)$ to particular values μ. EPI distributions maximize randomness via entropy, although other measures are sensible. D. Deep probability distributions map a latent random variable $\omega \sim q_0$, where q_0 is chosen to be simple distribution such as an isotropic gaussian, through a highly expressive function family $f_\theta(\omega) = f_l(...f_1(\omega))$ parameterized by the neural network weights and biases $\theta \in \Theta$. This mapping induces an implicit probability model $q(g_\theta(\omega)) \in \mathcal{Q}$

is the phenomenon of *network syncing* – in certain parameter regimes, the frequency of the hub neuron matches that of the fast and slow populations at an intermediate frequency. This emergent property is shown in Figure 1A at a frequency of 0.55Hz.

Third, qualitative parameter analysis ensues: since precise mathematical analysis is intractable in this model, a brute force sweep of parameters is done. Subsequently, a qualitative description is formulated to describe of the different parameter configurations that lead to the emergent property. In this last step lies the opportunity for a precise quantification of the emergent property as a statistical feature of the model. Once we have such a methodology, we can infer a probability distribution over parameter configurations that produce this emergent property.

Before presenting technical details (in the following section), let us understand emergent property inference schematically: the black box in Figure 1A takes, as input, the model and the specified emergent property, and produces as output the parameter distribution shown in Figure 1B. This distribution – represented for clarity as samples from the distribution – is then a scientifically meaningful and mathematically tractable object. It conveys parameter regions critical to the emergent property, directions in parameter space that will be invariant (or not) to that property, and more. In the STG model, this distribution can be specifically queried to determine the prototypical parameter configuration for network syncing (the mode; Figure 1B star), and then how quickly network syncing will decay based on changes away that mode. The inset of Figure 1B validates that indeed network syncing behaves as the distribution predicts, when moving away from the mode (Figure 1B star). Further validation of EPI is available in the supplementary materials, where we analyze a simpler model for which ground-truth statements can be made (Section A.1.1).

3.2 A deep generative modeling approach to emergent property inference

Emergent property inference (EPI) systematizes the three-step procedure of the previous section. First, we consider the model as a coupled set of differential (and potentially stochastic) equations [18]. In the running STG example, the dynamical state $x = [x_{\mathrm{f1}}, x_{\mathrm{f2}}, x_{\mathrm{hub}}, x_{\mathrm{s1}}, x_{\mathrm{s2}}]$ is the membrane potential for each neuron, which evolves according to the biophysical conductance-based equation:

$$C_m \frac{\partial x}{\partial t} = -h(x;z) = -\left[h_{leak}(x;z) + h_{Ca}(x;z) + h_K(x;z) + h_{hyp}(x;z) + h_{elec}(x;z) + h_{syn}(x;z)\right] \tag{1}$$

where C_m=1nF, and h_{leak}, h_{Ca}, h_K, h_{hyp}, h_{elec}, h_{syn} are the leak, calcium, potassium, hyperpolarization, electrical, and synaptic currents, all of which have their own complicated dependence on x

and $z = [g_{\text{el}}, g_{\text{synA}}]$ (see Section A.2.1).

Second, we define the emergent property, which as above is network syncing: the phase locking of the population and its oscillation at an intermediate frequency of our choosing (Figure 1A bottom). Quantifying this phenomenon is straightforward: we define network syncing to be that each neuron's spiking frequency – denoted $\omega_{\text{f1}}(x)$, $\omega_{\text{f2}}(x)$, etc. – is close to an intermediate frequency of 0.55Hz. Mathematically, we achieve this via constraints on the mean and variance of $\omega_i(x)$ for each neuron $i \in \{\text{f1}, \text{f2}, \text{hub}, \text{s1}, \text{s2}\}$, and thus:

$$E\left[T(x)\right] \triangleq E\begin{bmatrix} \omega_{\text{f1}}(x) \\ \vdots \\ (\omega_{\text{f1}}(x) - 0.55)^2 \\ \vdots \end{bmatrix} = \begin{bmatrix} 0.55 \\ \vdots \\ 0.025^2 \\ \vdots \end{bmatrix} \triangleq \mu, \tag{2}$$

which completes the quantification of the emergent property.

Third, we perform emergent property inference: we find a distribution over parameter configurations z, and insist that samples from this distribution produce the emergent property; in other words, they obey the constraints introduced in Equation 2. This distribution will be chosen from a family of probability distributions $\mathcal{Q} = \{q_\theta(z) : \theta \in \Theta\}$, defined by a deep generative distribution of the normalizing flow class [15, **?**, **?**] – neural networks which transform a simple distribution into a suitably complicated distribution (as is needed here). This deep distribution is represented in Figure 1E (and see Methods for more detail). Then, mathematically, we must solve the following optimization program:

$$\begin{aligned} &\underset{q_\theta \in \mathcal{Q}}{\text{argmax}}\, H(q_\theta(z)) \\ &\text{s.t. } E_{z\sim q_\theta}\left[E_{x\sim p(x|z)}\left[T(x)\right]\right] = \mu, \end{aligned} \tag{3}$$

where $T(x), \mu$ are defined as in Equation 3, and $p(x|z)$ is the intractable distribution of data from the model (x), given that model's parameters z (we access samples from this distribution by running the model forward). The purpose of each element in this program is detailed in Figure 1D. Finally, we recognize that many distributions in $\mathcal{Q}$ will respect the emergent property constraints, so we require a normative principle to select amongst them. This principle is captured in Equation 3 by the primal objective H. Here we chose Shannon entropy as a means to find parameter distributions with minimal assumptions beyond some chosen structure [26, 27, 16, 28], but we emphasize that the EPI method is unaffected by this choice (but the results of course will depend on this choice).

EPI optimizes the weights and biases θ of the deep neural network (which induces the probability

distribution) by iteratively solving Equation 3. The optimization is complete when the sampled models with parameters $z \sim q_\theta$ produce activity consistent with the specified emergent property. Such convergence is evaluated with a hypothesis test that the mean of each emergent property statistic is not different than its emergent property value (see Section A.1.2). Equipped with this method, we now prove out the value of EPI by using it to investigate three prominent models in neuroscience, using EPI to produce new insights about these models.

3.3 Comprehensive input-responsivity in a nonlinear sensory system

In studies of primary visual cortex (V1), theoretical models with excitatory (E) and inhibitory (I) populations have reproduced a host of experimentally documented phenomena. In particular regimes of excitation and inhibition, these E/I models exhibit the paradoxical effect [4], selective amplification [29], surround suppression [30], and sensory integrative properties [31]. Extending this model using experimental evidence of three genetically-defined classes of inhibitory neurons [32, 33], recent work [19] has investigated a four-population model – excitatory (E), parvalbumin (P), somatostatin (S), and vasointestinal peptide (V) neurons – as shown in Fig. 2A. The dynamical state of this model is the firing rate of each neuron-type population $x = [x_E, x_P, x_S, x_V]^\top$, which evolves according to rectified and exponentiated dynamics:

$$\tau \frac{dx}{dt} = -x + [Wx + h]_+^n \tag{4}$$

with effective connectivity weights W and input h. In our analysis, we set the time constant $\tau = 20$ms and dynamics coefficient $n = 2$. Also, as is fairly standard, we obtain an informative estimate of the effective connectivities between these neuron-types W in mice by multiplying their probability of connection with their average synaptic strength [**?**] (see Section A.2.2). Given these fixed choices of W, n, and τ, we studied the system's response to input

$$h = b + dh, \tag{5}$$

where the input h is comprised of a baseline input $b = [b_E, b_P, b_S, b_V]^\top$ and a differential input $dh = [dh_E, dh_P, dh_S, dh_V]^\top$ to each neuron-type population. Throughout subsequent analyses, the baseline input is $b = [1, 1, 1, 1]^\top$.

Having established our model, we now define the emergent property. We begin with the linearized response of the system $\frac{dx_{ss}}{dh}$ at a fixed point x_{ss}. While this linearization accurately predicts differential responses $dx_{ss} = [dx_{E,ss}, dx_{P,ss}, dx_{S,ss}, dx_{V,ss}]$ for small differential inputs to each population

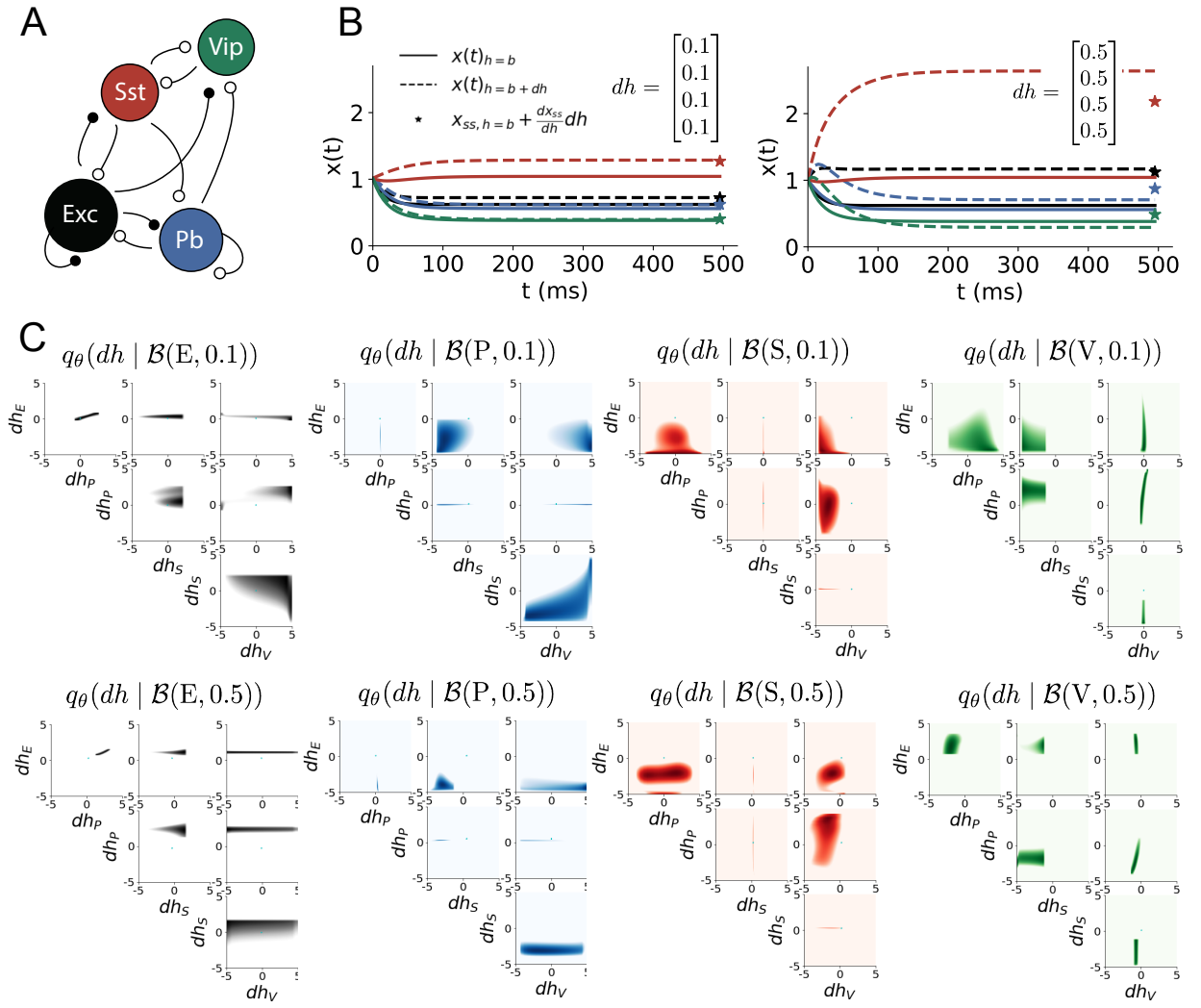

Figure 2: Exploring neuron-type responsivity in V1. A. Four-population model of primary visual cortex with excitatory (black), parvalbumin (blue), somatostatin (red), and vip (green) neurons. Some neuron-types largely do not form synaptic projections to others (excitatory and inhibitory projections filled and unfilled, respectively). B. Linear response predictions become inaccurate with greater input strength. V1 model simulations for input (solid) $h = b$ and (dashed) $h = b + dh$ with $b = [1, 1, 1, 1]\top$ and (left) $dh = [0.1, 0.1, 0.1, 0.1]\top$ (right) $dh = [0.5, 0.5, 0.5, 0.5]\top$. Stars indicate the linear response prediction. C. EPI distributions on differential input dh conditioned on differential response $\mathcal{B}(\alpha, y)$ (see text). The linear prediction from two standard deviations away from y (from negative to positive) is overlaid in cyan (very small, near origin).

$dh = [0.1, 0.1, 0.1, 0.1]$ (Fig. 2B, left), linearization is a poor predictor in this linear model more generally (Fig. 3B, right). Currently available approaches to deriving the steady state response of this system are limited.

To get a more comprehensive picture of the input-responsivity of each neuron-type, we used EPI to learn a distribution of differential inputs dh that cause the rate of each neuron-type population $\alpha \in \{E, P, S, V\}$ to increase by a value $y \in 0.1, 0.5$. These statements amount to the emergent property

$$\mathcal{B}(\alpha, y) \triangleq E\begin{bmatrix} dx_{\alpha,ss} \\ (dx_{\alpha,ss} - y)^2 \end{bmatrix} = \begin{bmatrix} y \\ 0.01^2 \end{bmatrix} \tag{6}$$

Note that we restrict the variance of the emergent property statistic $dx_{\alpha,ss}$ by constraining its variance to a small value. In Fig. 2C, each column visualizes the inferred distribution of dh corresponding to a specific neuron-type increase, while each row corresponds to amounts of increase 0.1 and 0.5. For visualization of this four-dimensional distribution, we show the two-dimensional marginal densities. The inferred distributions immediately suggest four hypotheses:

1. as is intuitive, each neuron-type's firing rate should be sensitive to that neuron-type's direct input;
2. the E- and P-populations should be largely unaffected by dh_V;
3. the S-population should be largely unaffected by dh_P;
4. EPI indicated that negative dh_E should result in small $dx_{V,ss}$, but positive dh_E should elicit a larger $dx_{V,ss}$; that is, there should be a nonmonotonic response of $dx_{V,ss}$ with dh_E.

We evaluate these hypotheses by taking steps in individual neuron-type input Δh_α away from the modes of the inferred distributions

$$dh^* = z^* = \underset{z}{\operatorname{argmax}} \log q_\theta(z \mid \mathcal{B}(\alpha, 0.1)) \tag{7}$$

Now, $dx_{\alpha,ss}$ is the steady state response to the system with input $h = b + dh^* + \Delta h_\alpha u_\alpha$ where u_α is a unit vector in the dimension of α. The EPI-generated hypotheses are confirmed.

- the neuron-type responses are sensitive to their direct inputs (Fig. 3A black, 3B blue, 3C red, 3D green);
- the E- and P-populations are not affected by dh_V (Fig. 3A green, 3B green);

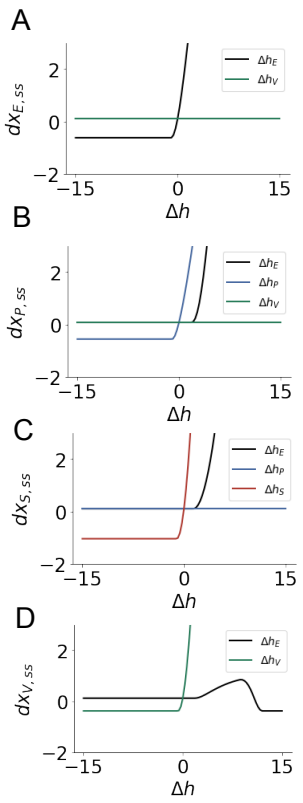

Figure 3: Confirming EPI generated hypotheses in V1. A. Differential responses by the E-population to changes in individual input $\Delta h_\alpha u_\alpha$ away from the mode of the EPI distribution dh^*. B-D Same plots for the P-, S-, and V-populations for the inputs for which hypotheses were formulated.

- the S-population is not affected by dh_P (Fig. 3C blue);
- the V-population has a nonmonotonic response to dh_E (Fig. 3D black).

These hypotheses were in stark contrast to what was available to us via traditional analytical linear prediction (Fig. 2C, cyan). To this point, we have shown the utility of EPI on relatively low-level emergent properties like network syncing and differential neuron-type population responses. In the remainder of the study, we focus on using EPI to understand models of more abstract cognitive function.

3.4 Identifying neural mechanisms of behavioral learning.

Identifying measurable biological changes that result in improved behavior is important for neuroscience, since they may indicate how the learning brain adapts. In a rapid task switching experiment [**?**], where rats were to respond right (R) or left (L) to the side of a light stimulus in the pro (P) task, and oppositely in the anti (A) task predicated by an auditory cue (Fig. 3A), neural recordings exhibited two population of neurons in each hemisphere of superior colliculus (SC) that simultaneously represented both task condition and motor response: the Pro/contralateral and

Anti/ipsilateral neurons [20]. Duan et al. proposed a model of SC that, like the V1 model analyzed in the previous section, is a four-population dynamical system. Here, the neuron-type populations are functionally-defined as the Pro- and Anti-populations in each hemisphere (left (L) and right (R)). The Pro- or Anti-populations receive an input determined by the cue, and then the left and right populations receive an input based on the side of the light stimulus. Activities were bounded between 0 and 1, so that a high output of the Pro population in a given hemisphere corresponds to the contralateral response. An additional stipulation is that when one Pro population responds with a high-output, the opposite Pro population must respond with a low output. Finally, this circuit operates in the presence of gaussian noise resulting in trial-to-trial variability (see Section A.2.3). The connectivity matrix is parameterized by the geometry of the population arrangement (Fig. 3B).

Here, we used EPI to learn distributions of the SC weight matrix parameters $z = W$ conditioned on of various levels of rapid task switching accuracy $\mathcal{B}(p)$ for $p \in \{50\%, 60\%, 70\%, 80\%, 90\%\}$ (see Section A.2.3). As is standard, we decomposed the connectivity matrix $W = QAQ^{-1}$ in such a way (the Schur decomposition) that the basis vectors q_i are the same for all W (Fig. 3C). These basis vectors have intuitive roles in processing for this task, and are accordingly named the *all* mode - all neurons co-fluctuate, *side* mode - one side dominates the other, *task* mode - the Pro or Anti populations dominate the other, and *diag* mode - Pro- and Anti-populations of opposite hemispheres dominate the opposite pair. The corresponding eigenvalues (e.g. a_{task}, which change according to W) indicate the degree to which activity along that mode is increased or decreased by W.

EPI demonstrates that, for greater task accuracies, the task mode eigenvalue increases, indicating the importance of W to the task representation (Fig. 4D, purple). Stepping from random chance (50%) networks to marginally task-performing (60%) networks, there is a marked decrease of the side mode eigenvalues (Fig. 3D, orange). Such side mode suppression remains in the models achieving greater accuracy, revealing its importance towards task performance. There were no interesting trends with learning in the all or diag mode (hence not shown in Fig. 3). Importantly, we can conclude from our methodology that side mode suppression in W allows rapid task switching, and that greater task-mode representations in W increase accuracy. These hypotheses are confirmed by forward simulation of the SC model (Fig. 3E). Thus, EPI produces novel, experimentally testable predictions: effective connectivity between these populations changes throughout learning, in a way that increases its task mode and decreases its side mode eigenvalues.

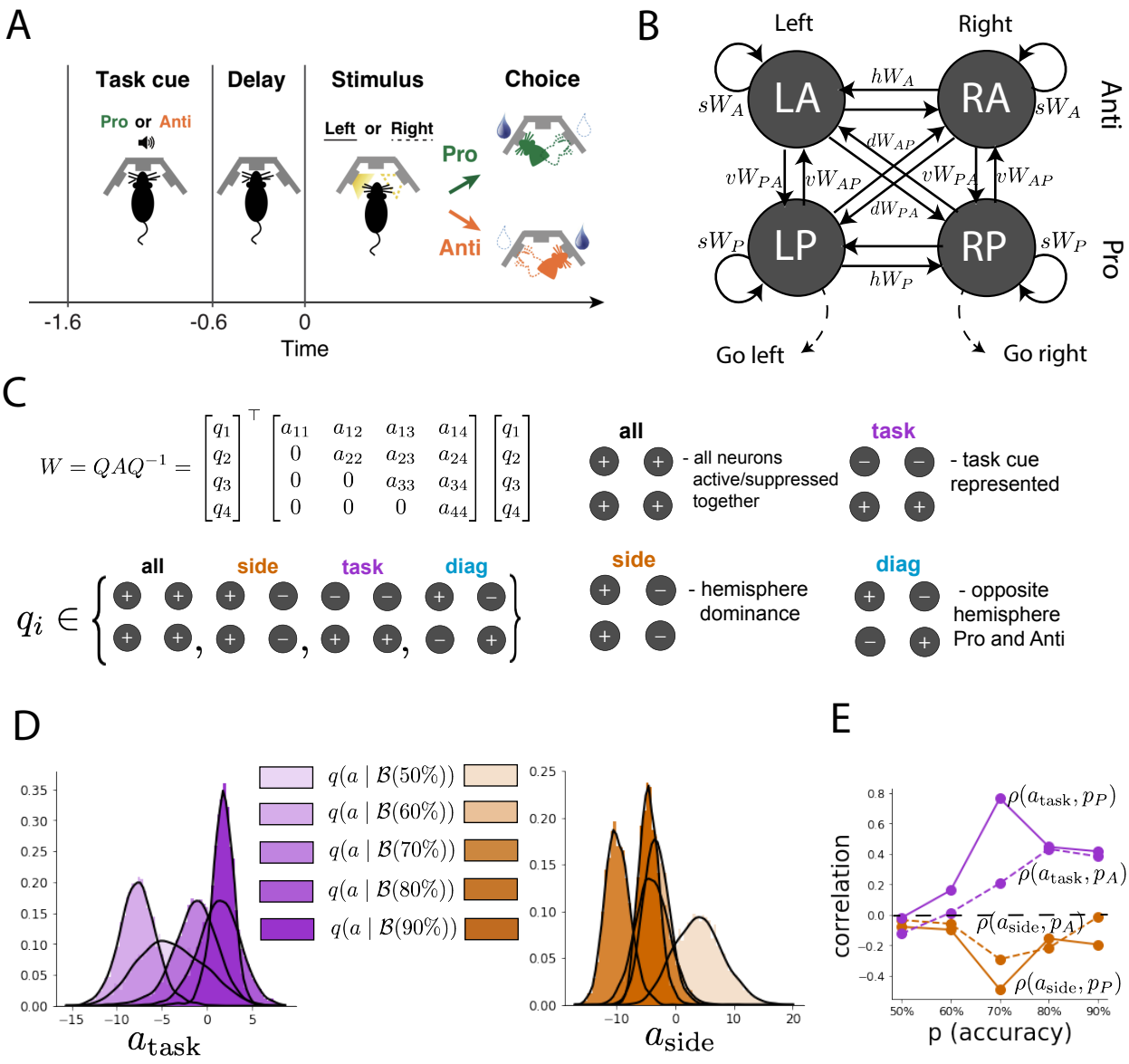

Figure 4: EPI reveals changes in SC [20] connectivity that result in greater task accuracy. A. Rapid task switching behavioral paradigm. In the Pro (Anti) condition indicated by an auditory cue, rats respond by poking into a side port to the same (opposite) side as the light stimulus that is provided after a delay to receive a reward. B. Model of superior colliculus (SC). Neurons: LP - left pro, RP - right pro, LA - left anti, RA - right anti. Parameters: sW - self, hW - horizontal, vW -vertical, dW - diagonal weights. C. The Schur decomposition of the weight matrix $W = QAQ^{-1}$ is a unique decomposition with orthogonal Q and upper triangular A. The invariant Schur modes are labeled by their hypothesized role in computation: q_{all}, q_{task}, q_{side}, and q_{diag}. The values of A are what change for different realizations of W. D. The marginal EPI distributions of the Schur eigenvalues at each level of task accuracy. E. The correlation of Schur eigenvalue with task performance in each learned EPI distribution.

3.5 Characterizing the sources of bias in RNN computation

Each model we thus far have studied was designed from fundamental biophysical principles, genetically- or functionally-defined neuron types. At a more abstract level of modeling, recurrent neural networks (RNNs) are high-dimensional models of computation and have become increasingly popular in neuroscience research [34]. Typically, RNNs are trained to do a task from a systems neuroscience experiment, and then the unit activations of the trained RNN are compared to recorded neural activity. Here we run EPI on the connectivity matrices of RNNs trained to solve a sample task.

Recent work establishes a link between RNN connectivity weights and the resulting dynamical responses of the network, using dynamic mean field theory (DMFT) [3]. Specifically, DMFT describes the properties of activity in infinite-size neural networks given a distribution on the connectivity weights. This theory has been extended from random neural networks to low-rank RNNs, which have low-dimensional parameterizations of RNN connectivity via the pairwise correlations of the low-rank vectors (i.e. the low-rank "geometry") [21]. In such a model, the connectivity of a rank-1 RNN's weight matrix J is the sum of a random component with strength determined by g and a structured component determined by the outer product of vectors m and n:

$$J = g\chi + \frac{1}{N}mn^\top, \tag{8}$$

where the activity x evolves as

$$\frac{\partial x}{\partial t} = -x(t) + J\phi(x(t)) + I(t), \tag{9}$$

and $I(t)$ is some input, ϕ is the tanh nonlinearity, and $\chi_{ij} \sim \mathcal{N}(0, \frac{1}{N})$. The entries of m and n are drawn from gaussian distributions $m_i \sim \mathcal{N}(M_m, 1)$ and $n_i \sim \mathcal{N}(M_n, 1)$.

Mastrogiuseppe et al. designed low-rank connectivities via the pairwise correlations of the vectors m, n in models that solve tasks from behavioral neuroscience. We can consider the DMFT equation solver as a black box that takes in a low-rank parameterization z (e.g. $z = [g, M_m, M_n]$) and outputs task-relevant response variables (e.g. average network activity μ, the temporal variability in the network Δ_T, or network activity along a given dimension κ). Importantly, the solution produced by the solver is differentiable with respect to the input parameters, allowing us to combine DMFT with EPI to learn distributions on such connectivity parameters of RNNs that execute tasks via an emergent property defined on the task-relevant responses produced by DMFT.

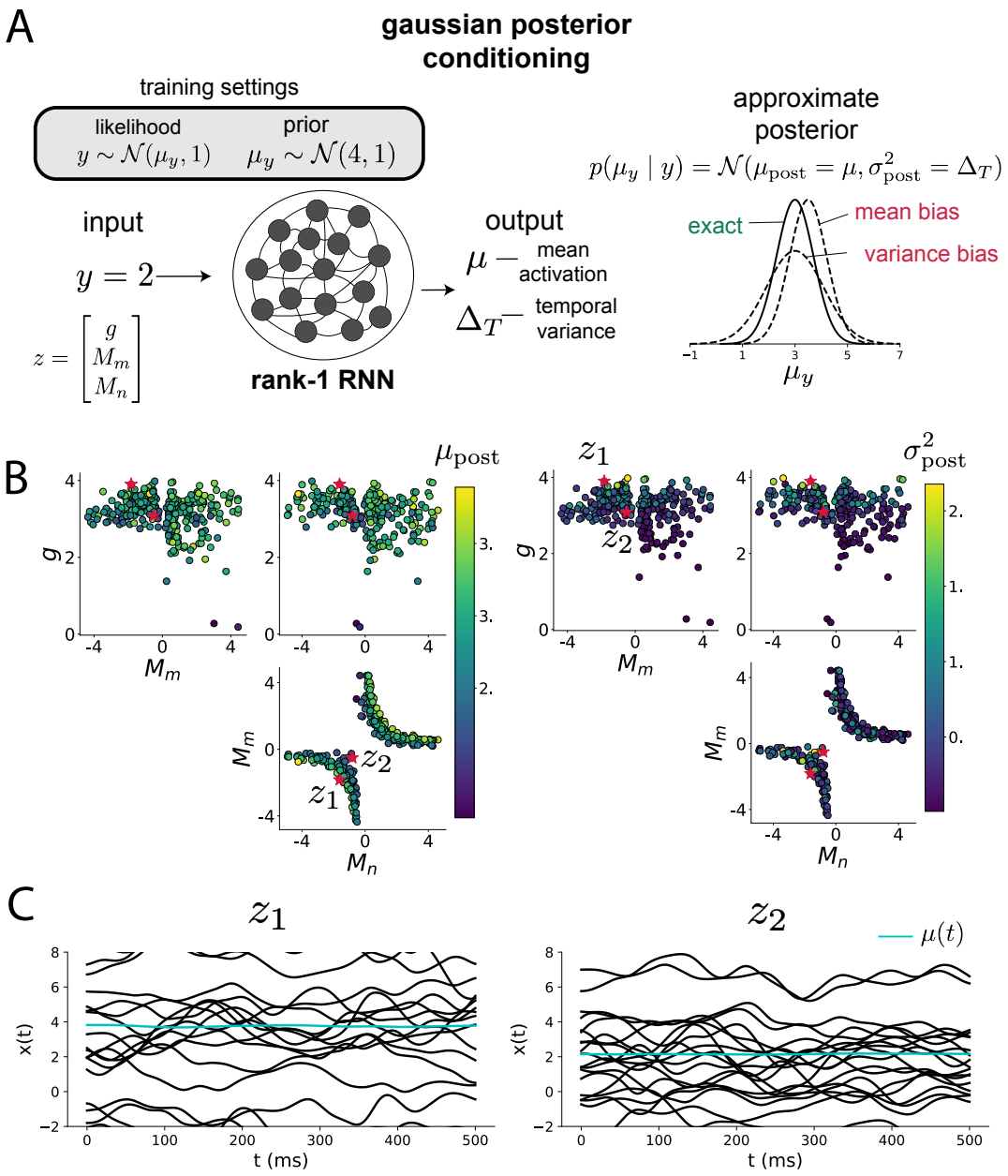

Figure 5: Sources of bias in RNN computation. A. (left) A rank-1 RNN running approximate Bayesian inference on μ_y assuming a gaussian likelihood variance of 1 and a prior of $\mathcal{N}(4, 1)$. (center) The rank-1 RNN represents the computed gaussian posterior mean μ_{post} and variance σ^2_{post} in its mean activity μ and its temporal variance Δ_T. (right) Bias in this computation can come from over- or under-estimating the posterior mean or variance. B. Distribution of rank-1 RNNs executing approximate Bayesian inference. Samples are colored by (left) posterior mean $\mu_{\text{post}} = \mu$ and (right) posterior variance $\sigma^2_{\text{post}} = \Delta_T$ C. Finite size realizations agree with the DMFT theory.

We train the network to solve gaussian posterior conditioning: calculate the parameters of a gaussian posterior distribution on the mean of a gaussian likelihood μ_y, given a single observation of $y \sim \mathcal{N}(\mu_y, 1)$ and a prior $p(\mu_y) = \mathcal{N}(4, 1)$ (Fig. 5A). The true posterior for an input of $y = 2$ is $p(\mu_y \mid y) = \mathcal{N}(3, 0.5)$. We used EPI to learn distributions of RNNs producing the correct posterior mean and variance in their mean activity $\mu = \mu_{\text{post}}$ and temporal variance $\Delta_T = \sigma^2_{\text{post}}$ (respectively), given an input of $y = 2$. (see Section A.2.4) (Fig. 5B).

When specifying the emergent property of gaussian posterior conditioning, we allowed a substantial amount of variability in the second moment constraints of the network mean μ and temporal variance Δ_T. This resulted in a distribution of rank-1 RNN parameterizations having a wide variety of biases in the resulting μ_{post} and σ^2_{post} (under- or over-estimates of the posterior means and variances). We can examine the nature of the biases in this computation by visualizing the produced posterior means (Fig. 5B, left) and variances (Fig. 5B, right) in the EPI distribution. The inferred distribution has rough symmetry in the M_m-M_n plane, suggesting a degeneracy in the product of M_m and M_n (Fig. 5B). The product of M_m and M_n almost completely determines the posterior mean (Fig. 5B, left), and the random strength g is the most influential variable on the temporal variance (Fig. 5B, right). Neither of these observations were obvious from the consistency equations afforded by DMFT (see Section A.2.4).

When working with DMFT, it's important to check that finite-size realizations of these infinite-size networks match the theoretical predictions. We check 2,000-neuron realizations of drawn parameters z_1 and z_2 from the inferred distribution. z_1 has relatively high g and high $M_m M_n$, whereas z_2 has relatively low g and low $M_m M_n$. Confirming our intuition, z_1 overestimates the posterior mean, since mean activity $\mu(t) > 3$ (Fig. 5C, left cyan). In turn, z_2 underestimates the posterior mean, since $\mu(t) < 3$ (Fig. 5C, right cyan). Finally, z_1 results in evidently greater temporal variance than z_2. This novel procedure of doing inference in interpretable parameterizations of RNNs conditioned on task execution is straightforwardly generalizable to other tasks like noisy integration and context-dependent decision making (Fig. S1).

4 Discussion

4.1 EPI is a general tool for theoretical neuroscience

Models of biological systems are often comprised of complex nonlinear differential equations, making traditional theoretical analysis and statistical inference intractable. In contrast, EPI is capable

of learning distributions of parameters in such models producing measurable signatures of computation. We have demonstrated its utility on biological models (STG), intermediate-level models of interacting genetically- and functionally-defined neuron-types (V1, SC), and the most abstract of models (RNNs). We are able to condition both deterministic and stochastic models on low-level emergent properties like firing rates of membrane potentials, as well as high-level cognitive function like gaussian posterior conditioning. Technically, EPI is tractable when the emergent property statistics are continuously differentiable with respect to the model parameters, which is very often the case; this emphasizes the general utility of EPI.

In this study, we have focused on applying EPI to low dimensional parameter spaces of models with low dimensional dynamical state. These choices were made to present the reader with a series of interpretable conclusions, which is more challenging in high dimensional spaces. In fact, EPI should scale reasonably to high dimensional parameter spaces, as the underlying technology has produced state-of-the-art performance on high-dimensional tasks such as texture generation [16]. Of course, increasing the dimensionality of the dynamical state of the model makes optimization more expensive, and there is a practical limit there as with any machine learning approach. For systems with high dimensional state, we recommend using theoretical approaches (e.g. [21]) to reason about reduced parameterizations of such high-dimensional systems.

There are additional technical considerations when assessing the suitability of EPI for a particular modeling question. First and foremost, as in any optimization problem, the defined emergent property should always be appropriately conditioned (constraints should not have wildly different units). Furthermore, if the program is underconstrained (not enough constraints), the distribution grows (in entropy) unstably unless mapped to a finite support. If overconstrained, there is no parameter set producing the emergent property, and EPI optimization will fail (appropriately). Next, one should consider the computational cost of the gradient calculations. In the best circumstance, there is a simple, closed form expression (e.g. Section A.1.1) for the emergent property statistic given the model parameters. On the other end of the spectrum, many forward simulation iterations may be required before a high quality measurement of the emergent property statistic is available (e.g. Section A.2.1). In such cases, optimization will be expensive.

4.2 Novel hypotheses from EPI

Machine learning has played an effective, multifaceted role in neuroscientific progress. Primarily, it has revealed structure in large-scale neural datasets [35, 36, 37, 38, 39, 40] (see review, [14]).

Secondarily, trained algorithms of varying degrees of biological relevance are beginning to be viewed as fully-observable computational systems comparable to the brain [41, 42].

For example, consider the fact that we do not fully understand the four-dimensional models of V1 [19]. Because analytical approaches to studying nonlinear dynamical systems become increasingly complicated when stepping from two-dimensional to three- or four-dimensional systems in the absence of restrictive simplifying assumptions [43], it is unsurprising that this model has been a challenge. In Section 3.3, we showed that EPI was far more informative about neuron-type input responsivity than the predictions afforded through analysis. By flexibly conditioning this V1 model on different emergent properties, we performed an exploratory analysis of a *model* rather than a dataset, which generated and proved out a set of testable predictions.

Of course, exploratory analyses can also be directed. For example, when interested in model changes during learning, one can use EPI to condition as we did in Section 3.4. This analysis identified experimentally testable predictions (proved out *in-silico*) of changes in connectivity in SC throughout learning. Precisely, we predict that an initial reduction in side mode eigenvalue, and a steady increase in task mode eigenvalue will take place, during learning, in the effective connectivity matrices of learning rats.

In our final analysis, we present a novel procedure for doing statistical inference on interpretable parameterizations of RNNs executing simple tasks. This methodology relies on recently extended theory of responses in random neural networks with minimal structure [21]. With this methodology, we can finally open the probabilistic model selection toolkit reasoning about the connectivity of RNNs solving tasks.

References

[1] Larry F Abbott. Theoretical neuroscience rising. *Neuron*, 60(3):489–495, 2008.

[2] John J Hopfield. Neurons with graded response have collective computational properties like those of two-state neurons. *Proceedings of the national academy of sciences*, 81(10):3088–3092, 1984.

[3] Haim Sompolinsky, Andrea Crisanti, and Hans-Jurgen Sommers. Chaos in random neural networks. *Physical review letters*, 61(3):259, 1988.

[4] Misha V Tsodyks, William E Skaggs, Terrence J Sejnowski, and Bruce L McNaughton. Paradoxical effects of external modulation of inhibitory interneurons. *Journal of neuroscience*, 17(11):4382–4388, 1997.

[5] Diederik P Kingma and Max Welling. Auto-encoding variational bayes. *International Conference on Learning Representations*, 2014.

[6] Danilo Jimenez Rezende, Shakir Mohamed, and Daan Wierstra. Stochastic backpropagation and variational inference in deep latent gaussian models. *International Conference on Machine Learning*, 2014.

[7] Yuanjun Gao, Evan W Archer, Liam Paninski, and John P Cunningham. Linear dynamical neural population models through nonlinear embeddings. In *Advances in neural information processing systems*, pages 163–171, 2016.

[8] Yuan Zhao and Il Memming Park. Recursive variational bayesian dual estimation for nonlinear dynamics and non-gaussian observations. *stat*, 1050:27, 2017.

[9] Gabriel Barello, Adam Charles, and Jonathan Pillow. Sparse-coding variational auto-encoders. *bioRxiv*, page 399246, 2018.

[10] Chethan Pandarinath, Daniel J O'Shea, Jasmine Collins, Rafal Jozefowicz, Sergey D Stavisky, Jonathan C Kao, Eric M Trautmann, Matthew T Kaufman, Stephen I Ryu, Leigh R Hochberg, et al. Inferring single-trial neural population dynamics using sequential auto-encoders. *Nature methods*, page 1, 2018.

[11] Alexander B Wiltschko, Matthew J Johnson, Giuliano Iurilli, Ralph E Peterson, Jesse M Katon, Stan L Pashkovski, Victoria E Abraira, Ryan P Adams, and Sandeep Robert Datta. Mapping sub-second structure in mouse behavior. *Neuron*, 88(6):1121–1135, 2015.

[12] Matthew J Johnson, David K Duvenaud, Alex Wiltschko, Ryan P Adams, and Sandeep R Datta. Composing graphical models with neural networks for structured representations and fast inference. In *Advances in neural information processing systems*, pages 2946–2954, 2016.

[13] Eleanor Batty, Matthew Whiteway, Shreya Saxena, Dan Biderman, Taiga Abe, Simon Musall, Winthrop Gillis, Jeffrey Markowitz, Anne Churchland, John Cunningham, et al. Behavenet: nonlinear embedding and bayesian neural decoding of behavioral videos. *Advances in Neural Information Processing Systems*, 2019.

[14] Liam Paninski and John P Cunningham. Neural data science: accelerating the experiment-analysis-theory cycle in large-scale neuroscience. *Current opinion in neurobiology*, 50:232–241, 2018.

[15] Danilo Jimenez Rezende and Shakir Mohamed. Variational inference with normalizing flows. *International Conference on Machine Learning*, 2015.

[16] Gabriel Loaiza-Ganem, Yuanjun Gao, and John P Cunningham. Maximum entropy flow networks. *International Conference on Learning Representations*, 2017.

[17] Dustin Tran, Rajesh Ranganath, and David Blei. Hierarchical implicit models and likelihood-free variational inference. In *Advances in Neural Information Processing Systems*, pages 5523–5533, 2017.

[18] Gabrielle J Gutierrez, Timothy O'Leary, and Eve Marder. Multiple mechanisms switch an electrically coupled, synaptically inhibited neuron between competing rhythmic oscillators. *Neuron*, 77(5):845–858, 2013.

[19] Ashok Litwin-Kumar, Robert Rosenbaum, and Brent Doiron. Inhibitory stabilization and visual coding in cortical circuits with multiple interneuron subtypes. *Journal of neurophysiology*, 115(3):1399–1409, 2016.

[20] Chunyu A Duan, Marino Pagan, Alex T Piet, Charles D Kopec, Athena Akrami, Alexander J Riordan, Jeffrey C Erlich, and Carlos D Brody. Collicular circuits for flexible sensorimotor routing. *bioRxiv*, page 245613, 2018.

[21] Francesca Mastrogiuseppe and Srdjan Ostojic. Linking connectivity, dynamics, and computations in low-rank recurrent neural networks. *Neuron*, 99(3):609–623, 2018.

[22] Sean R Bittner, Agostina Palmigiano, Kenneth D Miller, and John P Cunningham. Degenerate solution networks for theoretical neuroscience. *Computational and Systems Neuroscience Meeting (COSYNE), Lisbon, Portugal*, 2019.

[23] Sean R Bittner, Alex T Piet, Chunyu A Duan, Agostina Palmigiano, Kenneth D Miller, Carlos D Brody, and John P Cunningham. Examining models in theoretical neuroscience with degenerate solution networks. *Bernstein Conference*, 2019.

[24] Jan-Matthis Lueckmann, Pedro Goncalves, Chaitanya Chintaluri, William F Podlaski, Giacomo Bassetto, Tim P Vogels, and Jakob H Macke. Amortised inference for mechanistic models

of neural dynamics. In *Computational and Systems Neuroscience Meeting (COSYNE), Lisbon, Portugal*, 2019.

[25] Eve Marder and Vatsala Thirumalai. Cellular, synaptic and network effects of neuromodulation. *Neural Networks*, 15(4-6):479–493, 2002.

[26] Edwin T Jaynes. Information theory and statistical mechanics. *Physical review*, 106(4):620, 1957.

[27] Gamaleldin F Elsayed and John P Cunningham. Structure in neural population recordings: an expected byproduct of simpler phenomena? *Nature neuroscience*, 20(9):1310, 2017.

[28] Cristina Savin and Gašper Tkačik. Maximum entropy models as a tool for building precise neural controls. *Current opinion in neurobiology*, 46:120–126, 2017.

[29] Brendan K Murphy and Kenneth D Miller. Balanced amplification: a new mechanism of selective amplification of neural activity patterns. *Neuron*, 61(4):635–648, 2009.

[30] Hirofumi Ozeki, Ian M Finn, Evan S Schaffer, Kenneth D Miller, and David Ferster. Inhibitory stabilization of the cortical network underlies visual surround suppression. *Neuron*, 62(4):578–592, 2009.

[31] Daniel B Rubin, Stephen D Van Hooser, and Kenneth D Miller. The stabilized supralinear network: a unifying circuit motif underlying multi-input integration in sensory cortex. *Neuron*, 85(2):402–417, 2015.

[32] Henry Markram, Maria Toledo-Rodriguez, Yun Wang, Anirudh Gupta, Gilad Silberberg, and Caizhi Wu. Interneurons of the neocortical inhibitory system. *Nature reviews neuroscience*, 5(10):793, 2004.

[33] Bernardo Rudy, Gordon Fishell, SooHyun Lee, and Jens Hjerling-Leffler. Three groups of interneurons account for nearly 100% of neocortical gabaergic neurons. *Developmental neurobiology*, 71(1):45–61, 2011.

[34] Omri Barak. Recurrent neural networks as versatile tools of neuroscience research. *Current opinion in neurobiology*, 46:1–6, 2017.

[35] Robert E Kass and Valérie Ventura. A spike-train probability model. *Neural computation*, 13(8):1713–1720, 2001.

[36] Emery N Brown, Loren M Frank, Dengda Tang, Michael C Quirk, and Matthew A Wilson. A statistical paradigm for neural spike train decoding applied to position prediction from ensemble firing patterns of rat hippocampal place cells. *Journal of Neuroscience*, 18(18):7411–7425, 1998.

[37] Liam Paninski. Maximum likelihood estimation of cascade point-process neural encoding models. *Network: Computation in Neural Systems*, 15(4):243–262, 2004.

[38] M Yu Byron, John P Cunningham, Gopal Santhanam, Stephen I Ryu, Krishna V Shenoy, and Maneesh Sahani. Gaussian-process factor analysis for low-dimensional single-trial analysis of neural population activity. In *Advances in neural information processing systems*, pages 1881–1888, 2009.

[39] Kenneth W Latimer, Jacob L Yates, Miriam LR Meister, Alexander C Huk, and Jonathan W Pillow. Single-trial spike trains in parietal cortex reveal discrete steps during decision-making. *Science*, 349(6244):184–187, 2015.

[40] Lea Duncker, Gergo Bohner, Julien Boussard, and Maneesh Sahani. Learning interpretable continuous-time models of latent stochastic dynamical systems. *Proceedings of the 36th International Conference on Machine Learning*, 2019.

[41] David Sussillo and Omri Barak. Opening the black box: low-dimensional dynamics in high-dimensional recurrent neural networks. *Neural computation*, 25(3):626–649, 2013.

[42] Blake A Richards and et al. A deep learning framework for neuroscience. *Nature Neuroscience*, 2019.

[43] Steven H Strogatz. Nonlinear dynamics and chaos: with applications to physics. *Biology, Chemistry, and Engineering (Studies in Nonlinearity), Perseus, Cambridge, UK*, 1994.

[44] Rajesh Ranganath, Sean Gerrish, and David Blei. Black box variational inference. In *Artificial Intelligence and Statistics*, pages 814–822, 2014.

[45] Martin J Wainwright, Michael I Jordan, et al. Graphical models, exponential families, and variational inference. *Foundations and Trends® in Machine Learning*, 1(1–2):1–305, 2008.

[46] Laurent Dinh, Jascha Sohl-Dickstein, and Samy Bengio. Density estimation using real nvp. *Proceedings of the 5th International Conference on Learning Representations*, 2017.

[47] Carsten K Pfeffer, Mingshan Xue, Miao He, Z Josh Huang, and Massimo Scanziani. Inhibition of inhibition in visual cortex: the logic of connections between molecularly distinct interneurons. *Nature neuroscience*, 16(8):1068, 2013.

A Methods

A.1 Emergent property inference (EPI)

Emergent property inference (EPI) learns distributions of theoretical model parameters that produce emergent properties of interest. EPI combines ideas from likelihood-free variational inference [17] and maximum entropy flow networks [16]. A maximum entropy flow network is used as a deep probability distribution for the parameters, while these samples often parameterize a differentiable model simulator, which may lack a tractable likelihood function.

Consider model parameterization z and data x generated from some theoretical model simulator represented as $p(x \mid z)$, which may be deterministic or stochastic. Theoretical models usually have known sampling procedures for simulating activity given a circuit parameterization, yet often lack an explicit likelihood function due to the nonlinearities and dynamics. With EPI, a distribution on parameters z is learned, that yields an emergent property of interest $\mathcal{B}$,

$$\mathcal{B} \leftrightarrow E_{z\sim q_\theta}\left[E_{x\sim p(x|z)}\left[T(x)\right]\right] = \mu \tag{10}$$

by making an approximation $q_\theta(z)$ to $p(z \mid \mathcal{B})$ (see Section A.1.5). So, over the DSN distribution $q_\theta(z)$ of model $p(x \mid z)$ for behavior $\mathcal{B}$, the emergent properties $T(x)$ are constrained in expectation to μ.

In deep probability distributions, a simple random variable $w \sim p_0$ is mapped deterministically via a function f_θ parameterized by a neural network to the support of the distribution of interest where $z = f_\theta(\omega) = f_l(..f_1(\omega))$. Given a theoretical model $p(x \mid z)$ and some behavior of interest $\mathcal{B}$, the deep probability distributions are trained by optimizing the neural network parameters θ to find a good approximation q^*_θ within the deep variational family Q to $p(z \mid \mathcal{B})$.

In most settings (especially those relevant to theoretical neuroscience) the likelihood of the behavior with respect to the model parameters $p(T(x) \mid z)$ is unknown or intractable, requiring an alternative to stochastic gradient variational Bayes [5] or black box variational inference[44]. These types of methods called likelihood-free variational inference (LFVI, [17]) skate around the intractable likelihood function in situations where there is a differentiable simulator. Akin to LFVI, DSNs are

optimized with the following objective for a given theoretical model, emergent property statistics $T(x)$, and emergent property constraints μ:

$$\begin{aligned} q_\theta^*(z) &= \underset{q_\theta \in Q}{\operatorname{argmax}} H(q_\theta(z)) \\ &\text{s.t. } E_{z\sim q_\theta}\left[E_{x\sim p(x|z)}\left[T(x)\right]\right] = \mu \end{aligned} \tag{11}$$

Optimizing this objective is a technological accomplishment in its own right, the details of which we elaborate in Section A.1.2. Before going through those details, we ground this optimization in a toy example.

A.1.1 Example: 2D LDS

To gain intuition for EPI, consider two-dimensional linear dynamical systems, $\tau\dot{x} = Ax$ with

$$A = \begin{bmatrix} a_1 & a_2 \\ a_3 & a_4 \end{bmatrix}$$

that produce a band of oscillations. To do EPI with the dynamics matrix elements as the free parameters $z = [a_1, a_2, a_3, a_4]$, and fixing $\tau = 1$, such that the posterior yields a band of oscillations, the emergent property statistics $T(x)$ are chosen to contain the first- and second-moments of the oscillatory frequency Ω and the growth/decay factor d of the oscillating system. To learn the distribution of real entries of A that yield a distribution of d with mean zero with variance 0.25^2, and oscillation frequency Ω with mean 1 Hz with variance $(0.1\text{Hz})^2$, then we would select the real part of the complex conjugate eigenvalues $\text{real}(\lambda_1) = d$ (via an arbitrary choice of eigenvalue of the dynamics matrix λ_1) and the positive imaginary component of one of the eigenvalues $\text{imag}(\lambda_1) = 2\pi\Omega$ as the emergent property statistics. Those emergent property statistics are then constrained to

$$\mu = E\begin{bmatrix} \text{real}(\lambda_1) \\ \text{imag}(\lambda_1) \\ (\text{real}(\lambda_1) - 0)^2 \\ (\text{imag}(\lambda_1) - 2\pi\Omega)^2 \end{bmatrix} = \begin{bmatrix} 0.0 \\ 2\pi\Omega \\ 0.25^2 \\ (2\pi 0.1)^2 \end{bmatrix} \tag{12}$$

where $\Omega = 1\text{Hz}$. Unlike the models we study in the paper which calculate $E_{x\sim p(x|z)}\left[T(x)\right]$ via forward simulation, we have a closed form for the eigenvalues of the dynamics matrix. λ can be calculated using the quadratic formula:

$$\lambda = \frac{(\frac{a_1+a_4}{\tau}) \pm \sqrt{(\frac{a_1+a_4}{\tau})^2 + 4(\frac{a_2a_3 - a_1a_4}{\tau})}}{2} \tag{13}$$

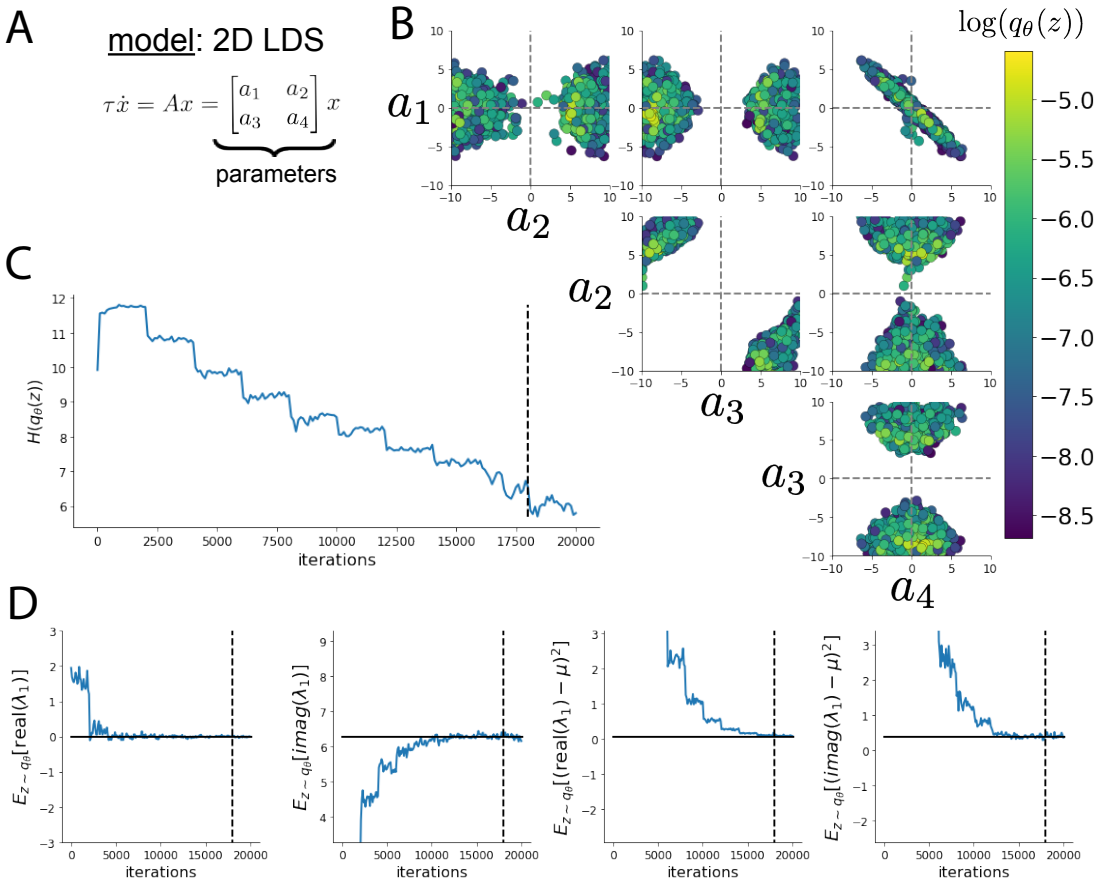

Fig. S2: A. Two-dimensional linear dynamical system model, where real entries of the dynamics matrix A are the parameters. B. The DSN distribution for a 2D LDS with $\tau = 1$ that produces an average of 1Hz oscillations with some small amount of variance. C. Entropy throughout the optimization. At the beginning of each augmented Lagrangian epoch (5,000 iterations), the entropy dips due to the shifted optimization manifold where emergent property constraint satisfaction is increasingly weighted. D. Emergent property moments throughout optimization. At the beginning of each augmented Lagrangian epoch, the emergent property moments move closer to their constraints.

where λ_1 is the eigenvalue of $\frac{1}{\tau}A$ with greatest real part. Even though $E_{x\sim p(x|z)}[T(x)]$ is calculable directly via a closed form function and does not require simulation, we cannot derive the distribution q_θ^* directly. This is due to the formally hard problem of the backward mapping: finding the natural parameters η from the mean parameters μ of an exponential family distribution [45]. Instead, we can use EPI to learn the linear system parameters producing such a band of oscillations (Fig. S2B).

Even this relatively simple system has nontrivial (though intuitively sensible) structure in the parameter distribution. To validate our method (further than that of the underlying technology on a ground truth solution [16]) we can analytically derive the contours of the probability density from the emergent property statistics and values (Fig. S3). In the $a_1 - a_4$ plane, is a black line at $\text{real}(\lambda_1) = \frac{a_1+a_4}{2} = 0$, a dotted black line at the standard deviation $\text{real}(\lambda_1) = \frac{a_1+a_4}{2} \pm 1$, and a grey line at twice the standard deviation $\text{real}(\lambda_1) = \frac{a_1+a_4}{2} \pm 2$ (Fig. S3A). Here the lines denote the set of solutions at fixed behaviors, which overlay the posterior obtained through EPI. The learned DSN distribution precisely reflects the desired statistical constraints and model degeneracy in the sum of a_1 and a_4. Intuitively, the parameters equivalent with respect to emergent property statistic $\text{real}(\lambda_1)$ have similar log densities.

To explain the structure in the bimodality of the DSN posterior, we can look at the imaginary component of λ_1. When $\text{real}(\lambda_1) = \frac{a_1+a_4}{2} = 0$, we have

$$\text{imag}(\lambda_1) = \begin{cases} \sqrt{\frac{a_1a_4 - a_2a_3}{\tau}}, & \text{if } a_1a_4 < a_2a_3 \\ 0 & \text{otherwise} \end{cases} \tag{14}$$

When $\tau = 1$ and $a_1a_4 > a_2a_3$ (center of distribution above), we have the following equation for the other two dimensions:

$$\text{imag}(\lambda_1)^2 = a_1a_4 - a_2a_3 \tag{15}$$

Since we constrained $E_{q_\theta}[\text{imag}(\lambda)] = 2\pi$ (with $\omega = 1$), we can plot contours of the equation $\text{imag}(\lambda_1)^2 = a_1a_4 - a_2a_3 = (2\pi)^2$ for various a_1a_4 (Fig. S3A). If $\sigma_{1,4} = E_{q_\theta}(|a_1a_4 - E_{q_\theta}[a_1a_4]|)$, then we plot the contours as $a_1a_4 = 0$ (black), $a_1a_4 = -\sigma_{1,4}$ (black dotted), and $a_1a_4 = -2\sigma_{1,4}$ (grey dotted) (Fig. S3B). This validates the curved structure of the inferred distribution learned through EPI. We take steps in negative standard deviation of a_1a_4 (dotted and gray lines), since there are few positive values a_1a_4 in the posterior. Subtler model-behavior combinations will have even more complexity, further motivating the use of EPI for understanding these systems. Indeed, we sample a distribution of systems oscillating near 1Hz (Fig. S4).

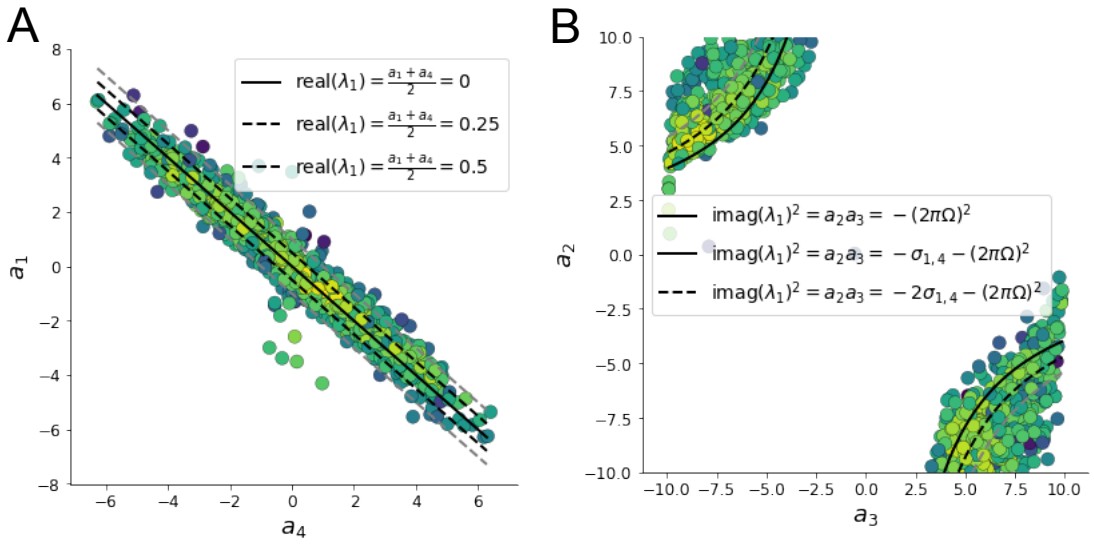

Fig. S3: A. Probability contours in the $a_1 - a_4$ plane can be derived from the relationship to emergent property statistic of growth/decay factor. B. Probability contours in the $a_2 - a_3$ plane can be derived from relationship to the emergent property statistic of oscillation frequency.

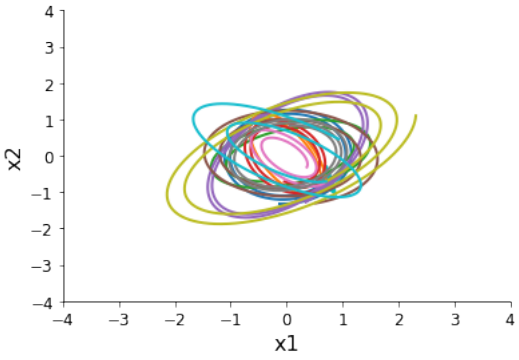

Fig. S4: Sampled dynamical system trajectories from the EPI distribution. Each trajectory is initialized at $x(0) = \begin{bmatrix} \frac{\sqrt{2}}{2} & -\frac{\sqrt{2}}{2} \end{bmatrix}$.

A.1.2 Augmented Lagrangian optimization

To optimize $q_\theta(z)$ in equation 1, the constrained optimization is performed using the augmented Lagrangian method. The following objective is minimized:

$$L(\theta; \alpha, c) = -H(q_\theta) + \alpha^\top \delta(\theta) + \frac{c}{2}||\delta(\theta)||^2 \tag{16}$$

where $\delta(\theta) = E_{z\sim q_\theta}\left[E_{x\sim p(x|z)}\left[T(x) - \mu\right]\right]$, $\alpha \in \mathcal{R}^m$ are the Lagrange multipliers and c is the penalty coefficient. For a fixed (α, c), θ is optimized with stochastic gradient descent. A low value of c is used initially, and increased during each augmented Lagrangian epoch – a period of optimization with fixed α and c for a given number of stochastic optimization iterations. Similarly, α is tuned each epoch based on the constraint violations. For the linear 2-dimensional system (Fig. S2C) optimization hyperparameters are initialized to $c_1 = 10^{-4}$ and $\alpha_1 = 0$. The penalty coefficient is updated based on a hypothesis test regarding the reduction in constraint violation. The p-value of $E[||\delta(\theta_{k+1})||] > \gamma E[||\delta(\theta_k)||]$ is computed, and c_{k+1} is updated to βc_k with probability $1 - p$. Throughout the project, $\beta = 4.0$ and $\gamma = 0.25$ is used. The other update rule is $\alpha_{k+1} = \alpha_k + c_k \frac{1}{n}\sum_{i=1}^{n}(T(x^{(i)}) - \mu)$. In this example, each augmented Lagrangian epoch ran for 2,000 iterations. We consider the optimization to have converged when a null hypothesis test of constraint violations being zero is accepted for all constraints at a significance threshold 0.05. This is the dotted line on the plots below depicting the optimization cutoff of EPI optimization for the 2-dimensional linear system. If the optimization is left to continue running, entropy usually decreases, and structural pathologies in the distribution may be introduced.

The intention is that c and α start at values encouraging entropic growth early in optimization. Then, as they increase in magnitude with each training epoch, the constraint satisfaction terms are increasingly weighted, resulting in a decrease in entropy. Rather than using a naive initialization, before EPI, we optimize the deep probability distribution parameters to generate samples of an isotropic gaussian of a selected variance, such as 1.0 for the 2D LDS example. This provides a convenient starting point, whose level of entropy is controlled by the user.

A.1.3 Normalizing flows

Since we are optimizing parameters θ of our deep probability distribution with respect to the entropy, we will need to take gradients with respect to the log-density of samples from the deep probability distribution.

$$H(q_\theta(z)) = \int -q_\theta(z)\log(q_\theta(z))dz = E_{z\sim q_\theta}\left[-\log(q_\theta(z))\right] = E_{\omega\sim q_0}\left[-\log(q_\theta(f_\theta(\omega)))\right] \tag{17}$$

$$\nabla_\theta H(q_\theta(z)) = E_{\omega\sim q_0}\left[-\nabla_\theta \log(q_\theta(f_\theta(\omega)))\right] \tag{18}$$

Deep probability models typically consist of several layers of fully connected neural networks. When each neural network layer is restricted to be a bijective function, the sample density can be calculated using the change of variables formula at each layer of the network. For $z' = f(z)$,

$$q(z') = q(f^{-1}(z'))\left|\det\frac{\partial f^{-1}(z')}{\partial z'}\right| = q(z)\left|\det\frac{\partial f(z)}{\partial z}\right|^{-1} \tag{19}$$

However, this computation has cubic complexity in dimensionality for fully connected layers. By restricting our layers to normalizing flows [15] – bijective functions with fast log determinant jacobian computations, we can tractably optimize deep generative models with objectives that are a function of sample density, like entropy. Most of our analyses use real NVP [46], which have proven effective in our architecture searches, and have the advantageous features of fast sampling and fast density evaluation.

A.1.4 Related work

(To come)

A.1.5 Emergent property inference as variational inference in an exponential family

(To come)

A.2 Theoretical models

In this study, we used emergent property inference to examine several models relevant to theoretical neuroscience. Here, we provide the details of each model and the related analyses.

A.2.1 Stomatogastric ganglion

Each neuron's membrane potential $x_m(t)$ is the solution of the following differential equation.

$$C_m \frac{\partial x_m}{\partial t} = -\left[h_{leak}(x;z) + h_{Ca}(x;z) + h_K(x;z) + h_{hyp}(x;z) + h_{elec}(x;z) + h_{syn}(x;z)\right] \tag{20}$$

The membrane potential of each neuron is affected by the leak, calcium, potassium, hyperpolarization, electrical and synaptic currents, respectively. The capacitance of the cell membrane was set to $C_m = 1nF$. Each current is a function of the neuron's membrane potential x_m and the parameters of the circuit such as g_{el} and g_{syn}, whose effect on the circuit is considered in the motivational example of EPI in Fig. 1. Specifically, the currents are the difference in the neuron's membrane potential and that current type's reversal potential multiplied by a conductance:

$$h_{leak}(x;z) = g_{leak}(x_m - V_{leak}) \tag{21}$$

$$h_{elec}(x;z) = g_{el}(x_m^{post} - x_m^{pre}) \tag{22}$$

$$h_{syn}(x;z) = g_{syn} S_\infty^{pre}(x_m^{post} - V_{syn}) \tag{23}$$

$$h_{Ca}(x;z) = g_{Ca} M_\infty (x_m - V_{Ca}) \tag{24}$$

$$h_K(x;z) = g_K N (x_m - V_K) \tag{25}$$

$$h_{hyp}(x;z) = g_h H (x_m - V_{hyp}) \tag{26}$$

The reversal potentials were set to $V_{leak} = -40mV$, $V_{Ca} = 100mV$, $V_K = -80mV$, $V_{hyp} = -20mV$, and $V_{syn} = -75mV$. The other conductance parameters were fixed to $g_{leak} = 1 \times 10^{-4}\mu S$. g_{Ca}, g_K, and g_{hyp} had different values based on fast, intermediate (hub) or slow neuron. Fast: $g_{Ca} = 1.9 \times 10^{-2}$, $g_K = 3.9 \times 10^{-2}$, and $g_{hyp} = 2.5 \times 10^{-2}$. Intermediate: $g_{Ca} = 1.7 \times 10^{-2}$, $g_K = 1.9 \times 10^{-2}$, and $g_{hyp} = 8.0 \times 10^{-3}$. Intermediate: $g_{Ca} = 8.5 \times 10^{-3}$, $g_K = 1.5 \times 10^{-2}$, and $g_{hyp} = 1.0 \times 10^{-2}$.

Furthermore, the Calcium, Potassium, and hyperpolarization channels have time-dependent gating dynamics dependent on steady-state gating variables M_∞, N_∞ and H_∞, respectively.

$$M_\infty = 0.5\left(1 + \tanh\left(\frac{x_m - v_1}{v_2}\right)\right) \tag{27}$$

$$\frac{\partial N}{\partial t} = \lambda_N (N_\infty - N) \tag{28}$$

$$N_\infty = 0.5\left(1 + \tanh\left(\frac{x_m - v_3}{v_4}\right)\right) \tag{29}$$

$$\lambda_N = \phi_N \cosh\left(\frac{x_m - v_3}{2v_4}\right) \tag{30}$$

$$\frac{\partial H}{\partial t} = \frac{(H_\infty - H)}{\tau_h} \tag{31}$$

$$H_\infty = \frac{1}{1 + \exp\left(\frac{x_m + v_5}{v_6}\right)} \tag{32}$$

$$\tau_h = 272 - \left(\frac{-1499}{1 + \exp\left(\frac{-x_m + v_7}{v_8}\right)}\right) \tag{33}$$

where we set $v_1 = 0mV$, $v_2 = 20mV$, $v_3 = 0mV$, $v_4 = 15mV$, $v_5 = 78.3mV$, $v_6 = 10.5mV$, $v_7 = -42.2mV$, $v_8 = 87.3mV$, $v_9 = 5mV$, and $v_{th} = -25mV$. These are the same parameter values used in [18].

Finally, there is a synaptic gating variable as well:

$$S_\infty = \frac{1}{1 + \exp\left(\frac{v_{th} - x_m}{v_9}\right)} \tag{34}$$

When the dynamic gating variables are considered, this is actually a 15-dimensional nonlinear dynamical system.

In order to measure the frequency of the hub neuron during EPI, the STG model was simulated for $T = 500$ time steps of $dt = 25ms$. In EPI, since gradients are taken throught the simulation process, the number of time steps are kept as modest if possible. The chosen dt and T were the most computationally convenient choices yielding accurate frequency measurement.

Our original approach to measuring frequency was to take the max of the fast Fourier transform (FFT) of the simulated time series. There are a few key considerations here. One is resolution in frequency space. Each FFT entry will correspond to a signal frequency of $\frac{F_s k}{N}$, where N is the number of samples used for the FFT, $F_s = \frac{1}{dt}$, and $k \in [0, 1, ..., N-1]$. Our resolution is improved by increasing N and decreasing dt. Increasing N = T-b, where b is some fixed number of buffer burn-in initialization samples, necessitates an increase in simulation time steps T, which directly increases computational cost. Increasing F_s (decreasing dt) increases system approximation accuracy, but requires more time steps before a full cycle is observed. At the level of $dt = 0.025$, thousands of temporal samples were required for resolution of .01Hz. These challenges in frequency resolution with the discrete Fourier transform motivated the use of an alternative basis of complex exponentials. Instead, we used a basis of complex exponentials with frequencies from 0.0-1.0 Hz at 0.01Hz resolution, $\Phi = [0.0, 0.01, ..., 1.0]^\top$

Another consideration was that the frequency spectra of the hub neuron has several peaks. This was due to high-frequency sub-threshold activity. The maximum frequency was often not the firing

frequency. Accordingly, subthreshold activity was set to zero, and the whole signal was low-pass filtered with a moving average window of length 20. The signal was subsequently mean centered. After this pre-processing, the maximum frequency in the filter bank accurately reflected the firing frequency.

Finally, to differentiate through the maximum frequency identification step, we used a sum-of-powers normalization strategy: Let $\mathcal{X}_i \in \mathcal{C}^{|\Phi|}$ be the complex exponential filter bank dot products with the signal $x_i \in \mathcal{R}^N$, where $i \in \{\text{f1}, \text{f2}, \text{hub}, \text{s1}, \text{s2}\}$. The "frequency identification" vector is

$$u_i = \frac{|\mathcal{X}_i|^\alpha}{\sum_{k=1}^{N} |\mathcal{X}_i(k)|^\alpha} \tag{35}$$

The frequency is then calculated as $\Omega_i = u_i^\top \Phi$ with $\alpha = 100$.

Network syncing, like all other emergent properties in this work, are defined by the emergent property statistics and values. The emergent property statistics are the first- and second-moments of the firing frequencies. The first moments are set to 0.55Hz, while the second moments are set to 0.025Hz^2.

$$E\begin{bmatrix} \Omega_{\text{f1}} \\ \Omega_{\text{f2}} \\ \Omega_{\text{hub}} \\ \Omega_{\text{s1}} \\ \Omega_{\text{s2}} \\ (\Omega_{\text{f1}} - 0.55)^2 \\ (\Omega_{\text{f2}} - 0.55)^2 \\ (\Omega_{\text{hub}} - 0.55)^2 \\ (\Omega_{\text{s1}} - 0.55)^2 \\ (\Omega_{\text{s2}} - 0.55)^2 \end{bmatrix} = \begin{bmatrix} 0.55 \\ 0.55 \\ 0.55 \\ 0.55 \\ 0.55 \\ 0.025^2 \\ 0.025^2 \\ 0.025^2 \\ 0.025^2 \\ 0.025^2 \end{bmatrix} \tag{36}$$

For EPI in Fig 2C, we used a real NVP architecture with two coupling layers. Each coupling layer had two hidden layers of 10 units each, and we mapped onto a support of $z \in \left[\begin{bmatrix} 0 \\ 0 \end{bmatrix}, \begin{bmatrix} 10 \\ 8 \end{bmatrix}\right]$ We have shown the EPI optimization that converged with maximum entropy across 2 random seeds and augmented Lagrangian coefficient initializations of c_0=0, 2, and 5.

A.2.2 Primary visual cortex

The dynamics of each neural populations average rate $x = \begin{bmatrix} x_E \\ x_P \\ x_S \\ x_V \end{bmatrix}$ are given by:

$$\tau \frac{dx}{dt} = -x + [Wx + h]_+^n \tag{37}$$

Some neuron-types largely lack synaptic projections to other neuron-types [47], and it is popular to only consider a subset of the effective connectivities [19].

$$W = \begin{bmatrix} W_{EE} & W_{EP} & W_{ES} & 0 \\ W_{PE} & W_{PP} & W_{PS} & 0 \\ W_{SE} & 0 & 0 & W_{SV} \\ W_{VE} & W_{VP} & W_{VS} & 0 \end{bmatrix} \tag{38}$$

Estimates of the of the probability of connection and strength of connection from the Allen institute result in an estimate of the effective connectivity [**?**]:

$$W = \begin{bmatrix} 0.0576 & 0.19728 & 0.13144 & 0 \\ 0.58855 & 0.30668 & 0.4285 & 0 \\ 0.15652 & 0 & 0 & 0.2 \\ 0.13755 & 0.0902 & 0.4004 & 0 \end{bmatrix} \tag{39}$$

We look at how this four-dimensional nonlinear dynamical model of V1 responds to different inputs, and compare the predictions of the linear response to the approximate posteriors obtained through EPI. The input to the system is the sum of a baseline input $b = \begin{bmatrix} 1 & 1 & 1 & 1 \end{bmatrix}^\top$ and a differential input dh:

$$h = b + dh \tag{40}$$

All simulations of this system had $T = 100$ time points, a time step $dt = 5$ms, and time constant $\tau = 20$ms. And the system was initialized to a random draw $x(0)_i \sim \mathcal{N}(1, 0.01)$.

We can describe the dynamics of this system more generally by

$$\dot{x}_i = -x_i + f(u_i) \tag{41}$$

where the input to each neuron is

$$u_i = \sum_j W_{ij} x_j + h_i \tag{42}$$

Let $F_{ij} = \gamma_i \delta(i,j)$, where $\gamma_i = f'(u_i)$. Then, the linear response is

$$\frac{\partial x_{ss}}{\partial h} = F(W\frac{\partial x_{ss}}{\partial h} + I) \tag{43}$$

which is calculable by

$$\frac{\partial x_{ss}}{\partial h} = (F^{-1} - W)^{-1} \tag{44}$$

The emergent property we considered was the first and second moments of the change in rate dx between the baseline input $h = b$ and $h = b + dh$. We use the following notation to indicate that the emergent property statistics were set to the following values:

$$\mathcal{B}(\alpha, y) \leftrightarrow E\begin{bmatrix} dx_{\alpha,ss} \\ (dx_{\alpha,ss} - y)^2 \end{bmatrix} = \begin{bmatrix} y \\ 0.01^2 \end{bmatrix} \tag{45}$$

In the final analysis for this model, we sweep the input one neuron at a time away from the mode of each inferred distributions $dh^* = z^* = \text{argmax}_z \log q_\theta(z \mid \mathcal{B}(\alpha, 0.1)$. The differential responses $dx_{\alpha,ss}$ are examined at perturbed inputs $h = b + dh^* + \Delta h_\alpha u_\alpha$ where u_α is a unit vector in the dimension of α and $\Delta h_\alpha \in [-15, 15]$.

For each $\mathcal{B}(\alpha, y)$ with $\alpha \in \{E, P, S, V\}$ and $y \in \{0.1, 0.5\}$, we ran EPI with five different random initial seeds using an architecture of four coupling layers, each with two hidden layers of 10 units. We set $c_0 = 10^5$. The support of the learned distribution was restricted to $z_i \in [-5, 5]$.

A.2.3 Superior colliculus

There are four total units: two in each hemisphere corresponding to the Pro/contralateral and Anti/ipsilateral populations. Each unit has an activity (x_i) and internal variable (u_i) related by

$$x_i(t) = \left(\frac{1}{2}\tanh\left(\frac{v_i(t) - \epsilon}{\zeta}\right) + \frac{1}{2}\right) \tag{46}$$

$\epsilon = 0.05$ and $\zeta = 0.5$ control the position and shape of the nonlinearity, repsectively.

We can order the elements of x_i and v_i into vectors x and v with elements

$$x = \begin{bmatrix} x_{LP} \\ x_{LA} \\ x_{RP} \\ x_{RA} \end{bmatrix} \qquad v = \begin{bmatrix} v_{LP} \\ v_{LA} \\ v_{RP} \\ v_{RA} \end{bmatrix} \tag{47}$$

721 The internal variables follow dynamics:

$$\tau \frac{\partial v}{\partial t} = -v + Wx + h + \sigma \partial B \tag{48}$$

722 with time constant $\tau = 0.09s$ and gaussian noise $\sigma \partial B$ controlled by the magnitude of $\sigma = 1.0$. The
723 weight matrix has 8 parameters sW_P, sW_A, vW_{PA}, vW_{AP}, hW_P, hW_A, dW_{PA}, and dW_{AP} (Fig.
724 4B).

$$W = \begin{bmatrix} sW_P & vW_{PA} & hW_P & dW_{PA} \\ vW_{AP} & sW_A & dW_{AP} & hW_A \\ hW_P & dW_{PA} & sW_P & vW_{PA} \\ dW_{AP} & hW_A & vW_{AP} & sW_A \end{bmatrix} \tag{49}$$

725 The system receives five inputs throughout each trial, which has a total length of 1.8s.

$$h = h_{\text{rule}} + h_{\text{choice-period}} + h_{\text{light}} \tag{50}$$

726 There are rule-based inputs depending on the condition,

$$h_{\text{P,rule}}(t) = \begin{cases} I_{\text{P,rule}} \begin{bmatrix} 1 & 0 & 0 & 1 \end{bmatrix}^\top, & \text{if } t \leq 1.2s \\ 0, & \text{otherwise} \end{cases} \tag{51}$$

727

$$h_{\text{A,rule}}(t) = \begin{cases} I_{\text{A,rule}} \begin{bmatrix} 0 & 1 & 1 & 0 \end{bmatrix}^\top, & \text{if } t \leq 1.2s \\ 0, & \text{otherwise} \end{cases} \tag{52}$$

728 a choice-period input,

$$h_{\text{choice}}(t) = \begin{cases} I_{\text{choice}} \begin{bmatrix} 1 & 1 & 1 & 1 \end{bmatrix}^\top, & \text{if } t > 1.2s \\ 0, & \text{otherwise} \end{cases} \tag{53}$$

729 and an input to the right or left-side depending on where the light stimulus is delivered.

$$h_{\text{light}}(t) = \begin{cases} I_{\text{light}} \begin{bmatrix} 1 & 1 & 0 & 0 \end{bmatrix}^\top, & \text{if } t > 1.2s \text{ and Left} \\ I_{\text{light}} \begin{bmatrix} 0 & 0 & 1 & 1 \end{bmatrix}^\top, & \text{if } t > 1.2s \text{ and Right} \\ 0, & t \leq 1.2s \end{cases} \tag{54}$$

730 The input parameterization was fixed to $I_{\text{P,rule}} = 10$, $I_{\text{A,rule}} = 10$, $I_{\text{choice}} = 2$, and $I_{\text{light}} = 1$

731 To produce a Bernoulli rate of p_{LP} in the Left, Pro condition (we can generalize this to either cue,
732 or stimulus condition), let $\hat{p}_i$ be the empirical average steady state (ss) response (final x_{LP} at end
733 of task) over M=500 gaussian noise draws for a given SC model parameterization z_i:

$$\hat{p}_i = E_{\sigma\partial B}\left[x_{LP,\text{ss}} \mid s = L, c = P, z_i\right] = \frac{1}{M}\sum_{j=1}^{M} x_{LP,\text{ss}}(s = L, c = P, z_i, \sigma\partial B_j) \tag{55}$$

For the first constraint, the average over posterior samples (from $q_\theta(z)$) to be p_{LP}:

$$E_{z_i\sim q_\phi}\left[E_{\sigma\partial B}\left[x_{LP,\text{ss}} \mid s = L, c = P, z_i\right]\right] = E_{z_i\sim q_\phi}\left[\hat{p}_i\right] = p_{LP} \tag{56}$$

We can then ask that the variance of the steady state responses across gaussian draws, is the Bernoulli variance for the empirical rate $\hat{p}_i$.

$$E_{z\sim q\phi}\left[\sigma^2_{err}\right] = 0 \tag{57}$$

$$\sigma^2_{err} = Var_{\sigma\partial B}\left[x_{LP,\text{ss}} \mid s = L, c = P, z_i\right] - \hat{p}_i(1 - \hat{p}_i) \tag{58}$$

We have an additional constraint that the Pro neuron on the opposite hemisphere should have the opposite value. We can enforce this with a final constraint:

$$E_{z\sim q\phi}\left[d_P\right] = 1 \tag{59}$$

$$E_{\sigma\partial W}\left[\left(x_{LP,\text{ss}} - x_{RP,\text{ss}}\right)^2 \mid s = L, c = P, z_i\right] \tag{60}$$

We refer to networks obeying these constraints as Bernoulli, winner-take-all networks. Since the maximum variance of a random variable bounded from 0 to 1 is the Bernoulli variance ($\hat{p}(1-\hat{p})$), and the maximum squared difference between to variables bounded from 0 to 1 is 1, we do not need to control the second moment of these test statistics. In reality, these variables are dynamical system states and can only exponentially decay (or saturate) to 0 (or 1), so the Bernoulli variance error and squared difference constraints can only be undershot. This is important to be mindful of when evaluating the convergence criteria. Instead of using our usual hypothesis testing criteria for convergence to the emergent property, we set a slack variable threshold for these technically infeasible constraints to 0.05.

Training DSNs to learn distributions of dynamical system parameterizations that produce Bernoulli responses at a given rate (with small variance around that rate) was harder to do than expected. There is a pathology in this optimization setup, where the learned distribution of weights is bimodal attributing a fraction p of the samples to an expansive mode (which always sends x_{LP} to 1), and a fraction $1-p$ to a decaying mode (which always sends x_{LP} to 0). This pathology was avoided using an inequality constraint prohibiting parameter samples that resulted in low variance of responses across noise.

In total, the emergent property of rapid task switching accuracy at level p was defined as

$$\mathcal{B}(p) \leftrightarrow \begin{bmatrix} \hat{p}_P \\ \hat{p}_A \\ (\hat{p}_P - p)^2 \\ (\hat{p}_A - p)^2 \\ \sigma^2_{P,err} \\ \sigma^2_{A,err} \\ d_P \\ d_A \end{bmatrix} = \begin{bmatrix} p \\ p \\ 0.15^2 \\ 0.15^2 \\ 0 \\ 0 \\ 1 \\ 1 \end{bmatrix} \tag{61}$$

For each accuracy level p, we ran EPI for 10 different random seeds and selected the maximum entropy solution using an architecture of 10 planar flows with $c_0 = 2$. The support of z was $\mathcal{R}^8$.

A.2.4 Rank-1 RNN

The network dynamics of neuron i's rate x evolve according to:

$$\dot{x}_i(t) = -x_i(t) + \sum_{j=1}^{N} J_{ij}\phi(x_j(t)) + I_i \tag{62}$$

where the connectivity is comprised of a random and structured component:

$$J_{ij} = g\chi_{ij} + P_{ij} \tag{63}$$

The random bulk component has elements drawn from $\chi_{ij} \sim \mathcal{N}(0, \frac{1}{N})$, and the structured component is a sum of r unit rank terms:

$$P_{ij} = \sum_{k=1}^{r} \frac{m_i^{(k)} n_j^{(k)}}{N} \tag{64}$$

Rank-1 vectors m and n have elements drawn

$$m_i \sim \mathcal{N}(M_m, \Sigma_m)$$

$$n_i \sim \mathcal{N}(M_n, \Sigma_n)$$

The current has the following statistics:

$$I = M_I + \frac{\Sigma_{mI}}{\Sigma_m} x_1 + \frac{\Sigma_{nI}}{\Sigma_n} x_2 + \Sigma_\perp h$$

where x_1, x_2, and h are standard normal random variables following the rank-1 input-driven example from [21].

We followed their prescription for deriving the consistency equations in the presence of chaos. The $\ddot{\Delta}$ equation is broken into the equation for Δ_0 and Δ_∞ by the autocorrelation dynamics assertions.

$$\ddot{\Delta(\tau)} = -\frac{\partial V}{\partial \Delta}$$

$$\ddot{\Delta} = \Delta - \{g^2\langle[\phi_i(t)\phi_i(t+\tau)]\rangle + \Sigma_m^2\kappa^2 + 2\Sigma_{mI}\kappa + \Sigma_I^2\}$$

We can write out the potential function by integrating the negated RHS.

$$V(\Delta, \Delta_0) = \int \mathcal{D}\Delta \frac{\partial V(\Delta, \Delta_0)}{\partial \Delta}$$

$$V(\Delta, \Delta_0) = -\frac{\Delta^2}{2} + g^2\langle[\Phi_i(t)\Phi_i(t+\tau)]\rangle + (\Sigma_m^2\kappa^2 + 2\Sigma_{mI}\kappa + \Sigma_I^2)\Delta + C$$

We assume that as time goes to infinity, the potential relaxes to a steady state.

$$\frac{\partial V(\Delta_\infty, \Delta_0)}{\partial \Delta} = -\Delta + \{g^2\langle[\phi_i(t)\phi_i(t+\infty)]\rangle + \Sigma_m^2\kappa^2 + 2\Sigma_{mI}\kappa + \Sigma_I^2\} = 0$$

$$\Delta_\infty = g^2\langle[\phi_i(t)\phi_i(t+\infty)]\rangle + \Sigma_m^2\kappa^2 + 2\Sigma_{mI}\kappa + \Sigma_I^2$$

This can be written more explicitly in terms of the gaussian integrals which are relatively (with respect to nongaussian distributions) cheap to evaluate.

$$\Delta_\infty = g^2 \int \mathcal{D}z \left[\int \mathcal{D}x\phi(\mu + \sqrt{\Delta_0 - \Delta_\infty}x + \sqrt{\Delta_\infty}z\right]^2 + \Sigma_m^2\kappa^2 + 2\Sigma_{mI}\kappa + \Sigma_I^2$$

Also, we assume that the energy of the system is preserved throughout the entirety of its evolution.

$$V(\Delta_0, \Delta_0) = V(\Delta_\infty, \Delta_0)$$

$$-\frac{\Delta_0^2}{2} + g^2\langle[\Phi_i(t)\Phi_i(t)]\rangle + (\Sigma_m^2\kappa^2 + 2\Sigma_{mI}\kappa + \Sigma_I^2)\Delta_0 + C = -\frac{\Delta_\infty^2}{2} + g^2\langle[\Phi_i(t)\Phi_i(t)]\rangle + (\Sigma_m^2\kappa^2 + 2\Sigma_{mI}\kappa + \Sigma_I^2)\Delta_\infty + C$$

We can arrange the terms into a difference of squares in Δ_0 and Δ_∞.

$$\frac{\Delta_0^2 - \Delta_\infty^2}{2} = g^2\left(\langle[\Phi_i(t)\Phi_i(t)]\rangle - \langle[\Phi_i(t)\Phi_i(t)]\rangle\right) + (\Sigma_m^2\kappa^2 + 2\Sigma_{mI}\kappa + \Sigma_I^2)(\Delta_0 - \Delta_\infty)$$

Similarly, we write out the resulting equation explicitly in terms of the gaussian integrals present.

$$\frac{\Delta_0^2 - \Delta_\infty^2}{2} = g^2\left(\int \mathcal{D}z\Phi^2(\mu + \sqrt{\Delta_0}z) - \int \mathcal{D}z \int \mathcal{D}x\Phi(\mu + \sqrt{\Delta_0 - \Delta_\infty}x + \sqrt{\Delta_\infty}z)\right)$$

$$+(\Sigma_m^2\kappa^2 + 2\Sigma_{mI}\kappa + \Sigma_I^2)(\Delta_0 - \Delta_\infty)$$

This results in a set of consistency equations for the dynamic mean field variables μ, κ, Δ_0, and Δ_∞. In order to obtain the values of these variables for a given parameterization, we must solve the following system of equations.

$$\begin{aligned}
\mu &= F(\mu, \kappa, \Delta_0, \Delta_\infty) = M_m \kappa + M_I \\
\kappa &= G(\mu, \kappa, \Delta_0, \Delta_\infty) = M_n \langle [\phi_i] \rangle + \Sigma_{nI} \langle \left[\phi_i'\right] \rangle \\
\frac{\Delta_0^2 - \Delta_\infty^2}{2} &= H(\mu, \kappa, \Delta_0, \Delta_\infty) = g^2 \left(\int \mathcal{D}z \Phi^2(\mu + \sqrt{\Delta_0} z) - \int \mathcal{D}z \int \mathcal{D}x \Phi(\mu + \sqrt{\Delta_0 - \Delta_\infty} x + \sqrt{\Delta_\infty} z) \right) \\
&\quad + (\Sigma_m^2 \kappa^2 + 2\Sigma_{mI} \kappa + \Sigma_I^2)(\Delta_0 - \Delta_\infty) \\
\Delta_\infty &= L(\mu, \kappa, \Delta_0, \Delta_\infty) = g^2 \int \mathcal{D}z \left[\int \mathcal{D}x \phi(\mu + \sqrt{\Delta_0 - \Delta_\infty} x + \sqrt{\Delta_\infty} z \right]^2 + \Sigma_m^2 \kappa^2 + 2\Sigma_{mI} \kappa + \Sigma_I^2
\end{aligned} \tag{65}$$

We can solve these equations by simulating the following Langevin dynamical system.

$$\begin{aligned}
x(t) &= \frac{\Delta_0(t)^2 - \Delta_\infty(t)^2}{2} \\
\Delta_0(t) &= \sqrt{2x(t) + \Delta_\infty(t)^2} \\
\dot{\mu}(t) &= -\mu(t) + F(\mu(t), \kappa(t), \Delta_0(t), \Delta_\infty(t)) \\
\dot{\kappa}(t) &= -\kappa + G(\mu(t), \kappa(t), \Delta_0(t), \Delta_\infty(t)) \\
\dot{x}(t) &= -x(t) + H(\mu(t), \kappa(t), \Delta_0(t), \Delta_\infty(t)) \\
\dot{\Delta_\infty}(t) &= -\Delta_\infty(t) + L(\mu(t), \kappa(t), \Delta_0(t), \Delta_\infty(t))
\end{aligned} \tag{66}$$

Then, the temporal variance, which is necessary for the gaussian posterio conditioning example, is simply calculated via

$$\Delta_T = \Delta_0 - \Delta_\infty \tag{67}$$

A.3 Supplementary Figures

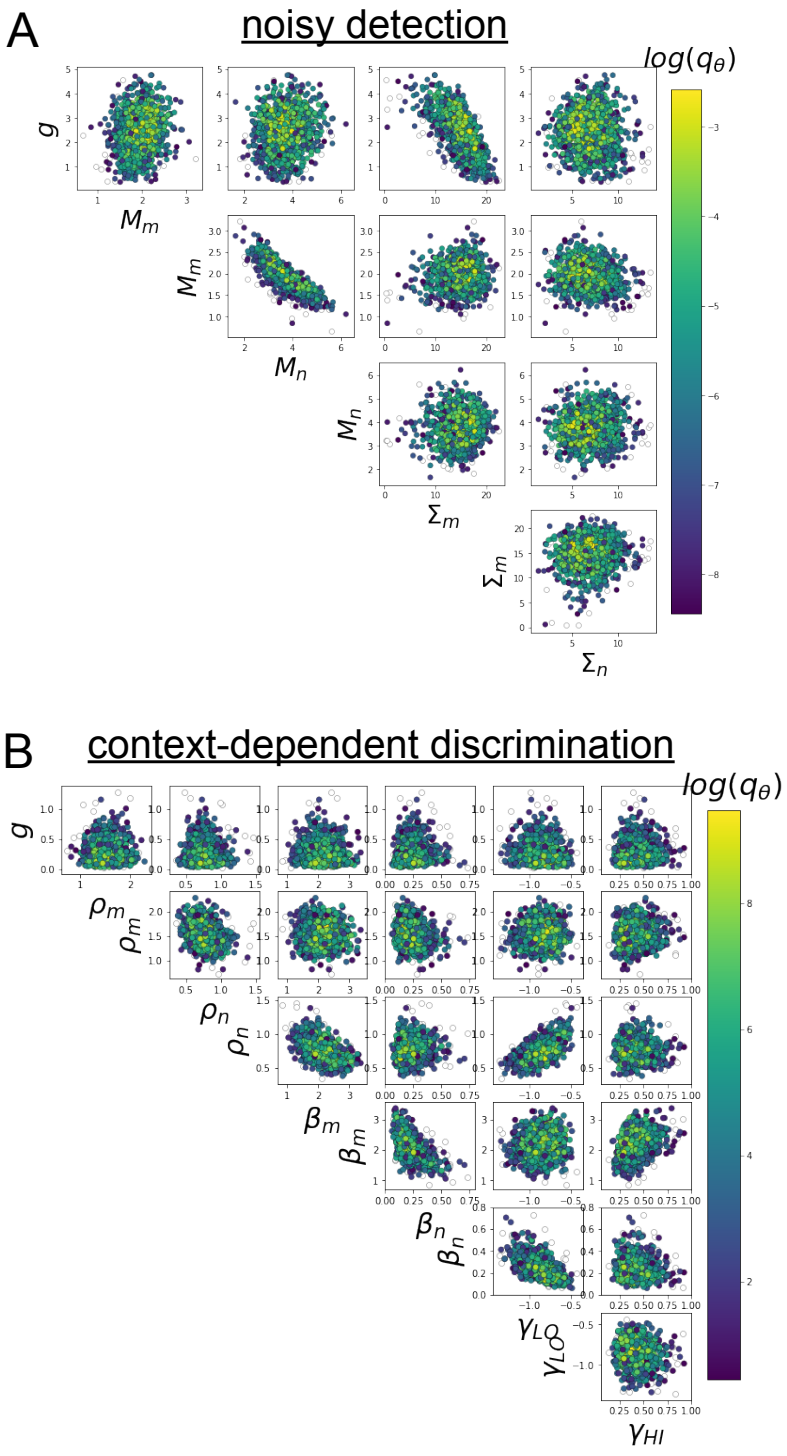

Fig. S1: A. EPI for rank-1 networks doing discrimination. B. EPI for rank-2 networks doing context-dependent discrimination.